Title	Osteoclasts adapt to physioxia perturbation through DNA demethylation
Author(s)	Nishikawa, Keizo; Seno, Shigeto; Yoshihara, Toshitada et al.
Citation	EMBO Reports. 2021, 22(12), p. e53035
Version Type	VoR
URL	https://hdl.handle.net/11094/93156
rights	This article is licensed under a Creative Commons Attribution-NonCommercial-NoDerivatives 4.0 International License.
Note	

Osteoclasts adapt to physioxia perturbation through DNA demethylation

Keizo Nishikawa[1,2,3,*] iD, Shigeto Seno[4] iD, Toshitada Yoshihara[5], Ayako Narazaki[3], Yuki Sugiura[6], Reito Shimizu[1], Junichi Kikuta[2,3,7], Reiko Sakaguchi[8,9], Norio Suzuki[10], Norihiko Takeda[11], Hiroaki Semba[11,12], Masamichi Yamamoto[13], Daisuke Okuzaki[14] iD, Daisuke Motooka[15], Yasuhiro Kobayashi[16], Makoto Suematsu[6], Haruhiko Koseki[17] iD, Hideo Matsuda[4] iD, Masayuki Yamamoto[18] iD, Seiji Tobita[5], Yasuo Mori[8,9,**] iD & Masaru Ishii[2,3,7,***] iD

Abstract

Oxygen plays an important role in diverse biological processes. However, since quantitation of the partial pressure of cellular oxygen *in vivo* is challenging, the extent of oxygen perturbation *in situ* and its cellular response remains underexplored. Using two-photon phosphorescence lifetime imaging microscopy, we determine the physiological range of oxygen tension in osteoclasts of live mice. We find that oxygen tension ranges from 17.4 to 36.4 mmHg, under hypoxic and normoxic conditions, respectively. Physiological normoxia thus corresponds to 5% and hypoxia to 2% oxygen in osteoclasts. Hypoxia in this range severely limits osteoclastogenesis, independent of energy metabolism and hypoxia-inducible factor activity. We observe that hypoxia decreases ten-eleven translocation (TET) activity. Tet2/3 cooperatively induces *Prdm1* expression via oxygen-dependent DNA demethylation, which in turn activates NFATc1 required for osteoclastogenesis. Taken together, our results reveal that TET enzymes, acting as functional oxygen sensors, regulate osteoclastogenesis within the physiological range of oxygen tension, thus opening new avenues for research on *in vivo* response to oxygen perturbation.

Introduction

Oxygen plays an essential role in serving as the final electron acceptor for aerobic respiration and is also a substrate in reactions that generate metabolites and structural macromolecules. Since a reduction in oxygen availability (hypoxia) has physiological and pathophysiological implications (Semenza, 2002; Palazon *et al*, 2014), aerobic organisms such as animals and land plants adopt alternative solutions to direct their primary hypoxia responses (Hammarlund *et al*, 2020). A major breakthrough in understanding such hypoxia responses in animals came through the discovery of the prolyl hydroxylase (PHD)/hypoxia-inducible factor (HIF) axis (Wang & Semenza, 1993; Maxwell *et al*, 1999; Ohh *et al*, 2000; Jaakkola *et al*,

2001). PHD enzymes are members of the 2-oxoglutarate (2-OG)-dependent dioxygenase enzyme family and act as oxygen sensors to catalyze the oxidation of specific prolyl residues in HIF-α proteins that enable their recognition by ubiquitin ligase complexes and their subsequent degradation by the proteasome. A decrease in oxygen availability results in the attenuation of PHD-mediated hydroxylation to enable HIF-α stabilization. The stabilized HIF-α can then heterodimerize with aryl hydrocarbon receptor nuclear translocator (ARNT) to trigger a genetic program that controls angiogenesis, cell growth, and a switch to a glycolytic cell metabolism, thereby enabling cellular adaptation to hypoxia (Semenza, 2002; Wilson *et al*, 2020).

Moreover, recent research on the hypoxia response machinery revealed the importance of other 2-OG-dependent dioxygenases whose activities also depend on oxygen availability. The DNA demethylases—ten-eleven translocation (TET) methylcytosine dioxygenases—catalyze the oxidation of 5-methylcytosine, but their activity is inhibited in severe hypoxic conditions of the tumor microenvironment, resulting in DNA hypermethylation (Laukka *et al*, 2016; Thienpont *et al*, 2016). The Jumonji-C (JmJC) domain-containing histone lysine demethylases (KDMs) also belong to the dioxygenase family of enzymes, which catalyze the oxidation of methyl groups on histones. Consequently, the hypoxia-induced decrease in the activity of KDMs leads to an altered histone methylation status, with implications for tumorigenesis (Batie *et al*, 2019; Chakraborty *et al*, 2019). These observations have raised intriguing questions as to which enzyme(s) play a pivotal role in oxygen sensing.

On the basis of the Michaelis–Menten constant (K_M) for oxygen, since each of the dioxygenases has a different affinity for oxygen [*e.g.*, KDM5A and KDM6A have a K_M of 117 and 260 mmHg, respectively (Batie *et al*, 2019; Chakraborty *et al*, 2019), TET2 has a K_M of 39 mmHg (Laukka *et al*, 2016), and PHD1 has a K_M ranging from 87 to 299 mmHg (Wilson *et al*, 2020)], the degree of changes in the reactions catalyzed by the dioxygenases largely depends on the factors that define hypoxia, which are in turn dependent on the tissue and intracellular concentration of oxygen in a given cell type. However, the extent of oxygen tension that a specific cell experiences *in vivo* still remains ambiguous.

Bone homeostasis depends on the intimate coupling of bone resorption by osteoclasts and bone formation by osteoblasts (Takayanagi, 2007; Lorenzo *et al*, 2008). Bone remodeling imbalance arising because of increased osteoclast activity and/or decreased osteoblast activity leads to bone-wasting states in diseases such as osteoporosis, rheumatoid arthritis, and periodontitis (Boyle *et al*, 2003; Teitelbaum & Ross, 2003; Zaidi, 2007). Glycolysis is the major metabolic pathway that regulates osteoblast differentiation, which is coordinated by the HIF-α proteins (Guntur *et al*, 2014; Regan *et al*, 2014; Dirckx *et al*, 2018). Indeed, hypoxia affects osteogenesis at a variety of levels ranging from direct action to indirect regulation via the stimulation of angiogenesis (Wang *et al*, 2007; Ramasamy *et al*, 2014; Xie *et al*, 2014). Thus, hypoxia is thought to provide a favorable environment for osteoblastogenesis (Lee *et al*, 2017). In contrast, oxidative metabolism is an oxygen-dependent energy-producing process that is essential for osteoclast differentiation (Ishii *et al*, 2009; Nishikawa *et al*, 2015). Of note, since bone resorption driven by the massive secretion of acids and specialized proteinases is an energy-consuming process, osteoclasts require substantial oxygen to support their energy demands with respect to

both differentiation and function. Thus, oxygen is likely to be an important environmental factor for osteoclast regulation; however, the *in vivo* oxygen tension in osteoclasts and the effect of its perturbation on osteoclastogenesis remain unclear.

Several methods to assess oxygen perturbation in different tissues are available. Immunohistochemistry for pimonidazole adducts and HIF-α accumulation is widely used for analyzing hypoxia within tissue (Varia *et al*, 1998; Ramasamy *et al*, 2014), but it is neither quantitative nor indicative of oxygen tension. Electrochemical electrodes are used to measure oxygen tension in real time; e.g., the tip of micro-electrode is positioned directly in the target tissue, and the electrode in the gas analyzer measures oxygen using the collected blood. However, these invasive procedures are not suitable for the measurement of oxygen tension in hard tissue. On the other hand, non-invasive methods to quantitatively assess oxygen tension *in vivo* have been developed based on phosphorescence quenching (Vanderkooi *et al*, 1987; Rumsey *et al*, 1988) and magnetic resonance techniques including magnetic resonance imaging (MRI), nuclear magnetic resonance (NMR), and electron paramagnetic resonance (EPR) (Roussakis *et al*, 2015). These methods have both advantages and limitations in terms of applicable targets, spatial resolution, tissue permeability, convenience, and reversibility. Of these methods, optical imaging utilizing a phosphorescence probe has great advantages in determining the spatio-temporal dynamics of oxygen in both soft and hard tissues (Spencer *et al*, 2014; Hirakawa *et al*, 2015; Yoshihara *et al*, 2015). Here, using two-photon phosphorescence lifetime imaging microscopy with a cell-penetrating phosphorescent probe that we originally developed, we first succeeded in determining the physiological range of oxygen tension in the bone marrow at the single-cell resolution. Furthermore, we show that TET enzymes play a pivotal role in oxygen sensing and are involved in osteoclastogenesis via an epigenetic regulation mechanism within the physiological range of oxygen tension.

Results

Definition of physiological normoxia and hypoxia for osteoclasts in the local bone marrow environment of live mice

Phosphorescence quenching by oxygen is a standard method for the sequential monitoring and non-invasive measurement of oxygen concentration (Vanderkooi *et al*, 1987; Rumsey *et al*, 1988). We recently developed a method to assess intracellular oxygen tension using a cell-penetrating phosphorescent probe (BTPDM1) based on the Ir (III) complex and a bifurcated fiber system (Hirakawa *et al*, 2015). The current study used a two-photon laser scanning microscope (TPLSM) equipped with time-correlated single-photon counting (TCSPC) system, to assess combined intensity-lifetime imaging of phosphorescence in live mice. This technique was named two-photon phosphorescence lifetime imaging microscopy (2PLIM). Prior to imaging, BTPDM1 was injected into *Tcirg*^GFP/+^ mice, their osteoclast lineage cells of which express green fluorescence protein (GFP) (Sun-Wada *et al*, 2009). GFP fluorescence enabled osteoclasts to be visualized while the phosphorescence lifetime was simultaneously measured using the TCSPC system (Fig 1A and B). The phosphorescence lifetime of mice osteoclasts during air inhalation was 2.98 ± 0.02 μs (Fig 1C). In order to calculate oxygen tension of

osteoclasts via phosphorescence lifetime, we prepared a calibration curve showing the relationship between phosphorescence lifetime and oxygen concentration (Fig EV1A and B). We cultured primary osteoclasts treated with BTPDM1 and measured phosphorescence lifetime under various oxygen concentrations. The results indicated that the *in vivo* oxygen tension of osteoclasts was 36.4 ± 0.7 mmHg ($4.8 \pm 0.1\%$; Figs 1D and EV1C). Next, in order to determine the physiological range of oxygen tension in osteoclasts, we measured the oxygen tension of osteoclasts in mice during hypoxic air inhalation (approximately 14% oxygen to reduce arterial oxygen saturation [spO_2] to 55%). As a result, phosphorescence lifetime of osteoclasts in these mice was prolonged to 3.62 ± 0.03 μs, which in turn was estimated as 17.4 ± 0.6 mmHg ($2.3 \pm 0.1\%$) of oxygen tension (Figs 1E and EV1C). These results enabled us to introduce a physiological context to oxygen tension of osteoclasts *in vivo*, i.e., ca. 5% as physiological normoxia (referred to as physioxia) in the mice whose spO_2 is 98% during air inhalation and ca. 2% as physiological hypoxia in the mice whose spO_2 reduced to 55% during inhalation of hypoxic air containing 14% oxygen.

Studies that have been conducted so far on the effect of hypoxia on osteoclast differentiation indicate that oxygen is a negative regulator of osteoclast differentiation (Arnett *et al*, 2003; Fukuoka *et al*, 2005; Murata *et al*, 2017). Osteoclast differentiation was evaluated *in vitro* by counting multinucleated cells (MNCs) positive for the osteoclast marker, tartrate-resistant acid phosphatase (TRAP), following stimulation of bone marrow-derived monocyte/macrophage precursor cells (BMMs) with receptor activator of nuclear factor-κB ligand (RANKL), and in the presence of macrophage colony-stimulating factor (M-CSF)(Nishikawa *et al*, 2010; Hayashi *et al*, 2012). We confirmed that the formation of TRAP-positive MNCs was significantly enhanced when they were cultured in hypoxic conditions of 10% oxygen, compared with that under atmospheric air conditions (Appendix Fig S1A). However, our 2PLIM revealed that these culture conditions do not reflect *in vivo* oxygen levels. In order to mimic *in vivo* oxygen tension, we investigated the effect of hypoxia on osteoclast differentiation by performing an *in vitro* experiment either in 5% oxygen (physioxia) or 2% oxygen (hypoxia). The experiment produced results contrary to those of previous results. The formation of TRAP-positive MNCs was severely impaired under 2% oxygen compared with that under 5% oxygen (Fig 1F and Appendix Fig S1B). Nevertheless, neither the number of proliferative BMMs nor the apoptotic activities of BMMs were affected in both 5% and 2% oxygen (Appendix Fig S1C and D). These results suggest that oxygen is a positive regulator of osteoclast differentiation.

The effect of hypoxia on bone metabolism was studied *in vivo* by studying an experimental mouse hypoxia models generated under acute (oxygen inhalation at a low concentration) conditions. Mice exposed to hypoxia displayed high bone mass phenotypes with low numbers of osteoclasts, while no obvious difference in the number of osteoblasts was observed (Fig 2A–C). Although the hypoxia signaling pathway is involved in the promotion of osteoblastogenesis (Wang *et al*, 2007), our experimental conditions, wherein the mice were exposed to 14% oxygen for 10 days, did not affect osteoblastogenesis. Taken together, these results suggest that hypoxia causes high bone mass due to defective osteoclast differentiation.

HIF-α is dispensable for the osteoclast response to physioxia perturbation

The above-stated findings raised the necessity for elucidating the mechanism(s) underlying oxygen-induced regulation of osteoclast differentiation. Hypoxia-inducible transcription factors, HIF-1α and HIF-2α, are the key mediators of cellular adaptation to oxygen deprivation (Wang *et al*, 1995). PHDs, members of the 2-oxoglutarate-dependent dioxygenase family, play a well-established role as oxygen sensors during the hydroxylation of specific proline residues on HIFs. This leads to their destabilization via ubiquitination induced by von-Hippel Lindau (VHL) ubiquitin ligase and subsequent proteasomal degradation under oxygen-rich conditions (Majmundar *et al*, 2010). Both osteoclast precursors and mature osteoclasts expressed HIF-related molecules (Appendix Fig S2A). In addition, protein expression of HIF-1α and HIF-2α under 2% oxygen was compared with that under 5% oxygen (Fig 3A). Therefore, we hypothesized that HIFs may be involved in the impairment of osteoclast differentiation under physiological hypoxia. We crossed *Hif1a-flox/flox* and *Hif2aflox/flox* mice (Ryan *et al*, 1998, 2000; Semba *et al*, 2016) with *Rank^Cre/+* (Maeda *et al*, 2012) mice to specifically disrupt *Hif1a* and *Hif2a* in the osteoclast lineage ($Hif1a_{Rank}^{-/-}$; $Hif2a_{Rank}^{-/-}$). However, no obvious difference in RANKL-induced formation of TRAP-positive MNCs and the expression of osteoclast-related genes was observed between the wild-type and $Hif1a_{Rank}^{-/-}$; $Hif2a_{Rank}^{-/-}$ cells under both 2% and 5% oxygen, although the expression of HIF-target genes was severely decreased in $Hif1a_{Rank}^{-/-}$; $Hif2a_{Rank}^{-/-}$ cells (Fig 3A–C). Furthermore, $Hif1a_{Rank}^{-/-}$; $Hif2a_{Rank}^{-/-}$ mice exposed to hypoxia displayed high bone mass phenotypes with a decreased number of osteoclasts, similar to that of the wild-type mice (Fig 2). These results suggested that HIFs were not involved in hypoxia-induced inhibition of osteoclast differentiation.

Energy metabolism in osteoclasts is not affected by physioxia perturbation

It has also been proposed that mitochondrial oxidative phosphorylation acts as an oxygen sensor to produce adenosine triphosphate (ATP) by transferring electrons to oxygen (Solaini *et al*, 2010). Indeed, intracellular ATP levels in osteoclasts are heavily dependent on mitochondrial activity (Nishikawa *et al*, 2015). We therefore hypothesized that hypoxia may perturb energy metabolism, leading to the inhibition of osteoclast differentiation. In order to examine the effect of hypoxia on ATP generation in osteoclasts *in vivo*, we used a genetically encoded ATP biosensor, GO-ATeam2 (Nakano *et al*, 2011; Yamamoto *et al*, 2019), to visualize ATP levels in osteoclasts. As GO-ATeam2 is composed of a bacteria-derived ATP binding domain sandwiched between EGFP and orange fluorescent protein (OFP), as the Förster resonance energy transfer (FRET) pair, specific binding of ATP to the GO-ATeam2 domain induces a conformational change that leads to FRET between the two fluorophores. As a quantitative FRET readout, we measured the fluorescence lifetime of EGFP from GO-ATeam2 in live mice using a TPLSM with TCSPC imaging technique (two-photon fluorescence lifetime imaging microscopy, 2FLIM) and calculated the FRET efficiency of GO-ATeam2 based on the fluorescence lifetime measurement. We generated mice expressing GO-ATeam2 and tdTomato proteins in osteoclast lineage cells by crossing *ROSA26^GO-ATeam2/+* (Yamamoto
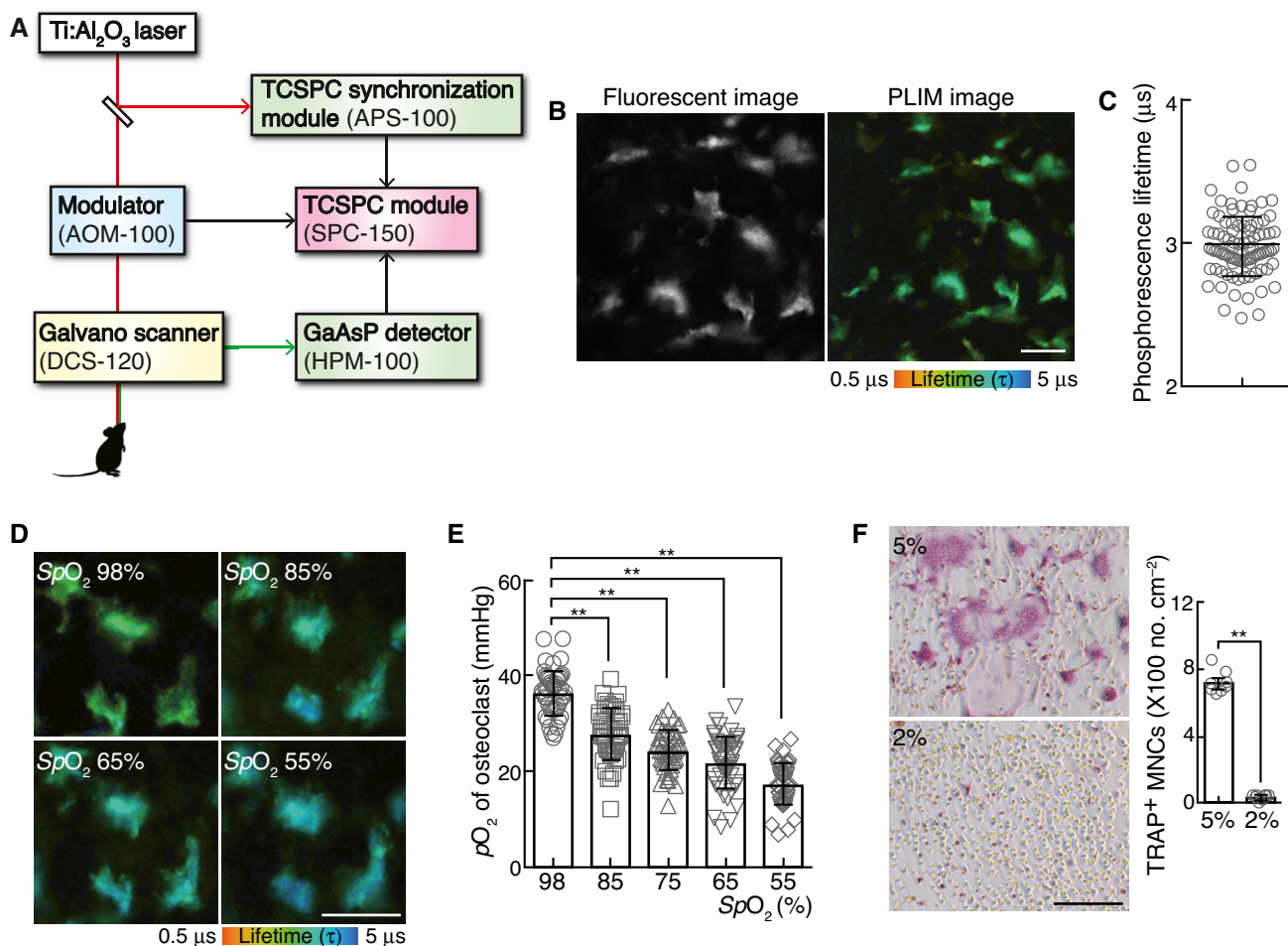
Figure 1. Measurement of passive physiological range of oxygen tension (pO_2) of osteoclasts.

A   Schematic diagram of the two-photon intravital imaging and 2PLIM.
B   Representative intravital image of calvarial bone marrow of $Tcirg1^{EGFP/+}$ male mice treated with BTPDM1 showing osteoclasts (left, EGFP fluorescence) and 2PLIM image for pO_2 changes (right, phosphorescence lifetime of BTPDM1). Scale bar, 20 μm.
C   Phosphorescence lifetime in each osteoclast of calvarial bone marrow of mice upon exposure to ambient air ($n = 91$ from six mice). Data denote mean ± s.e.m.
D, E   Change in pO_2 of osteoclasts in the mice upon exposure to various concentrations of oxygen from 21% to 14% pO_2. Magnified PLIM images of osteoclasts under different peripheral oxygen saturations (SpO_2, D). The pO_2 of each osteoclast in these mice was plotted (E, n = 47 from three mice for each SpO_2). Scale bar, 20 μm. Data denote mean ± s.e.m. **$P < 0.01$ (ANOVA).
F   Effect of physioxia (5% pO_2) or physiological hypoxia (2% pO_2) on osteoclastogenesis. TRAP-stained cells (left panel) and the number of TRAP-positive cells with more than three nuclei (right). Scale bar, 100 μm. Data denote mean ± s.e.m. **$P < 0.01$ ($n = 8$ biological replicates; t-test).

et al, 2019) mice with $Tg(Acp5\text{-}tdTomato)$ mice (Kikuta et al, 2013). The fluorescence of the tdTomato protein enabled the visualization of osteoclasts, while fluorescence lifetime was simultaneously measured using the TCSPC system. The FRET efficiency of GO-ATeam2 in mouse osteoclasts during air inhalation was 0.40 ± 0.02 (Fig 4A). Next, to determine the effect of hypoxia on osteoclast ATP levels, we performed fluorescence lifetime measurements in mice during hypoxic air inhalation. The FRET efficiency of GO-ATeam2 in mouse osteoclasts was almost comparable to that of mice during air inhalation, suggesting that ATP metabolism in osteoclasts remains unaffected within the physiological range of oxygen in vivo.

Nicotinamide adenosine dinucleotide (NAD^+) is a key determinant of cellular energy metabolism, while $NADP^+$, its

phosphorylated form, plays a central role in biosynthetic pathways and redox regulation. Both are reduced to form NAD(P)H and have identical spectral properties and emit autofluorescence upon excitation. NAD(P)H has both short and long autofluorescence lifetimes, depending on whether it is in a free or protein-bound state. In general, free and protein-bound states of NAD(P)H reflect glycolysis and oxidative phosphorylation, respectively. Therefore, the decrease in autofluorescence lifetime of NAD(P)H is attributed to a shift from oxidative phosphorylation to glycolysis (Kalinina et al, 2016). In order to further investigate the role of hypoxia on energy metabolism in osteoclasts in vivo, we employed autofluorescence lifetime imaging of NAD(P)H in $Tg(Acp5\text{-}tdTomato)$ mice. The fluorescence of tdTomato protein enabled osteoclasts to be visualized while autofluorescence lifetime was being
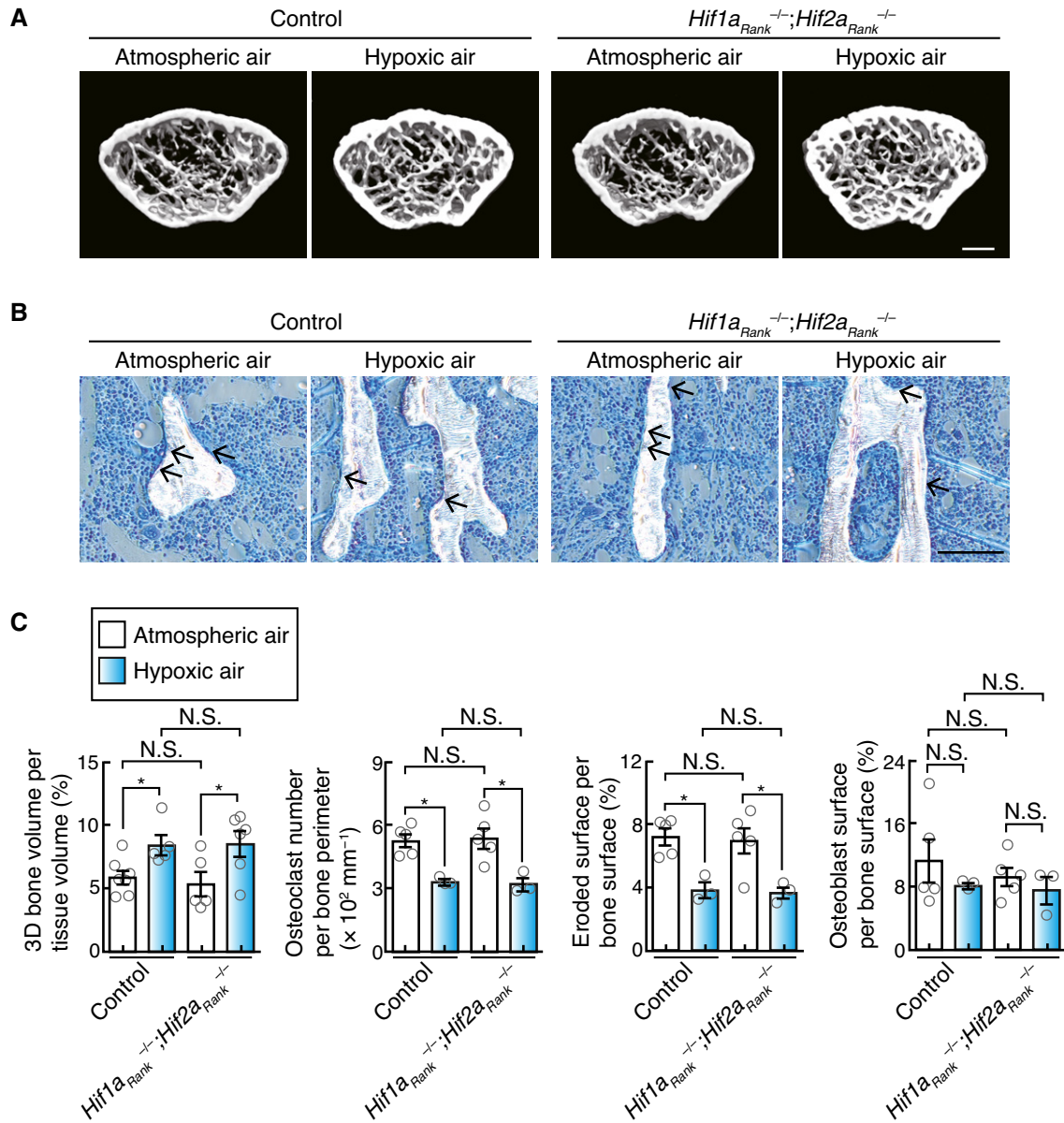
Figure 2. Effect of oxygen deprivation on bone metabolism.

A μCT analysis of the femurs of 10-week-old male mice upon exposure to low oxygen concentration (14% pO_2, $n = 5$) or ambient air ($n = 7$), and of 10-week-old $Hif1a_{Rank}^{-/-}$; $Hif2a_{Rank}^{-/-}$ male mice upon exposure to low oxygen concentration (14% pO_2, $n = 6$) or ambient air ($n = 5$) for 10 days (axial view of the metaphyseal region). Scale, 0.5 mm.

B Histological analysis of the proximal tibias of 10-week-old male mice upon exposure to low oxygen concentration (14% pO_2) or ambient air for 10 days, and of 10-week-old $Hif1a_{Rank}^{-/-}$; $Hif2a_{Rank}^{-/-}$ male mice upon exposure to low oxygen concentration (14% pO_2) or ambient air (toluidine blue staining [arrow, osteoclasts]). Scale, 100 μm.

C Parameters for osteoclasts and osteoblasts during bone morphometric analysis of 10-week-old male mice under low oxygen concentration ($n = 3$) or ambient air ($n = 5$), and 10-week-old $Hif1a_{Rank}^{-/-}$; $Hif2a_{Rank}^{-/-}$ male under low oxygen concentration ($n = 3$) or ambient air ($n = 5$) for 10 days. Data denote mean ± s.e.m. *$P < 0.05$; NS, not significant (t-test).

simultaneously measured using the TCSPC system. The average autofluorescence lifetime of osteoclasts in mice during air inhalation was 1.49 ± 0.02 ns (Fig 4B). Next, to determine the effect of hypoxia on osteoclast energy metabolism, we measured autofluorescence lifetime during hypoxic air inhalation by mice. The

average autofluorescence lifetime in hypoxic mouse osteoclasts was almost comparable to that of mice during air inhalation. These results indicated that cellular energy metabolism in osteoclasts was not affected within the physiological range of oxygen tension *in vivo*.
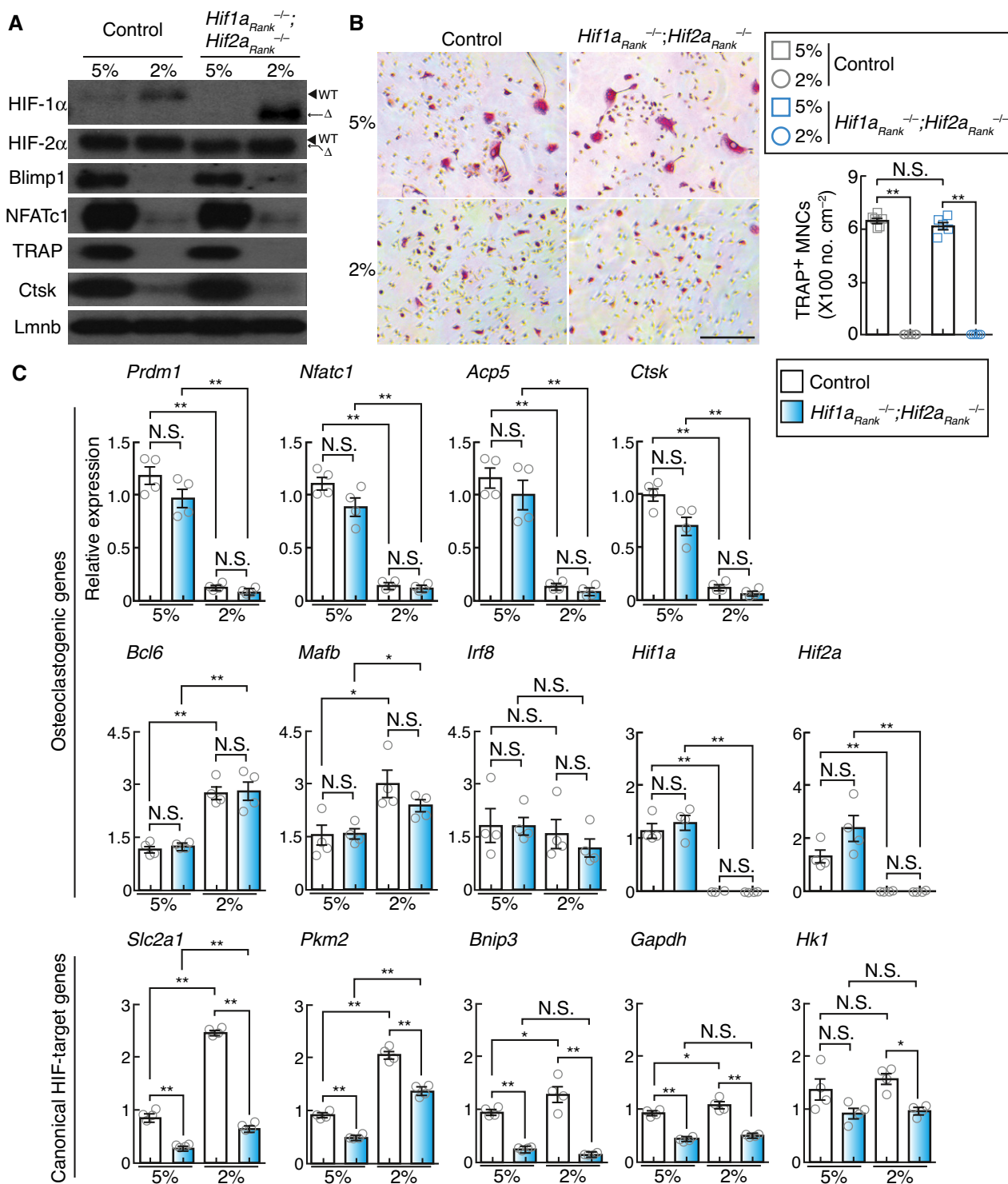
Figure 3. Effect of physiological hypoxia on hypoxia-inducible factor activity.

A Protein expression of HIF-1α, HIF-2α, Blimp1, NFATc1, Ctsk, and TRAP in control and *Hif1a$_{Rank}$$^{-/-}$; Hif2a$_{Rank}$$^{-/-}$* BMMs stimulated with RANKL and cultured under different conditions of oxygen concentration for 2 days.

B Effect of physioxia (5% *p*O$_2$) or physiological hypoxia (2% *p*O$_2$) on the formation of osteoclast from control and *Hif1a$_{Rank}$$^{-/-}$; Hif2a$_{Rank}$$^{-/-}$* BMMs. TRAP-stained cells (left panel) and the number of TRAP-positive cells with more than three nuclei (right). Scale bar, 100 μm. Data denote mean ± s.e.m. **$P < 0.01$; NS, not significant (*n* = 6 (control) and *n* = 6 (*Hif1a$_{Rank}$$^{-/-}$; Hif2a$_{Rank}$$^{-/-}$*) biological replicates; ANOVA).

C Expression of osteoclastogenic and canonical HIF-target genes in wild-type control and *Hif1a$_{Rank}$$^{-/-}$; Hif2a$_{Rank}$$^{-/-}$* BMMs under conditions of 5% or 2% oxygen. Data denote mean ± s.e.m. *$P < 0.05$; **$P < 0.01$; NS, not significant (*n* = 4 biological replicates; ANOVA).

A

B
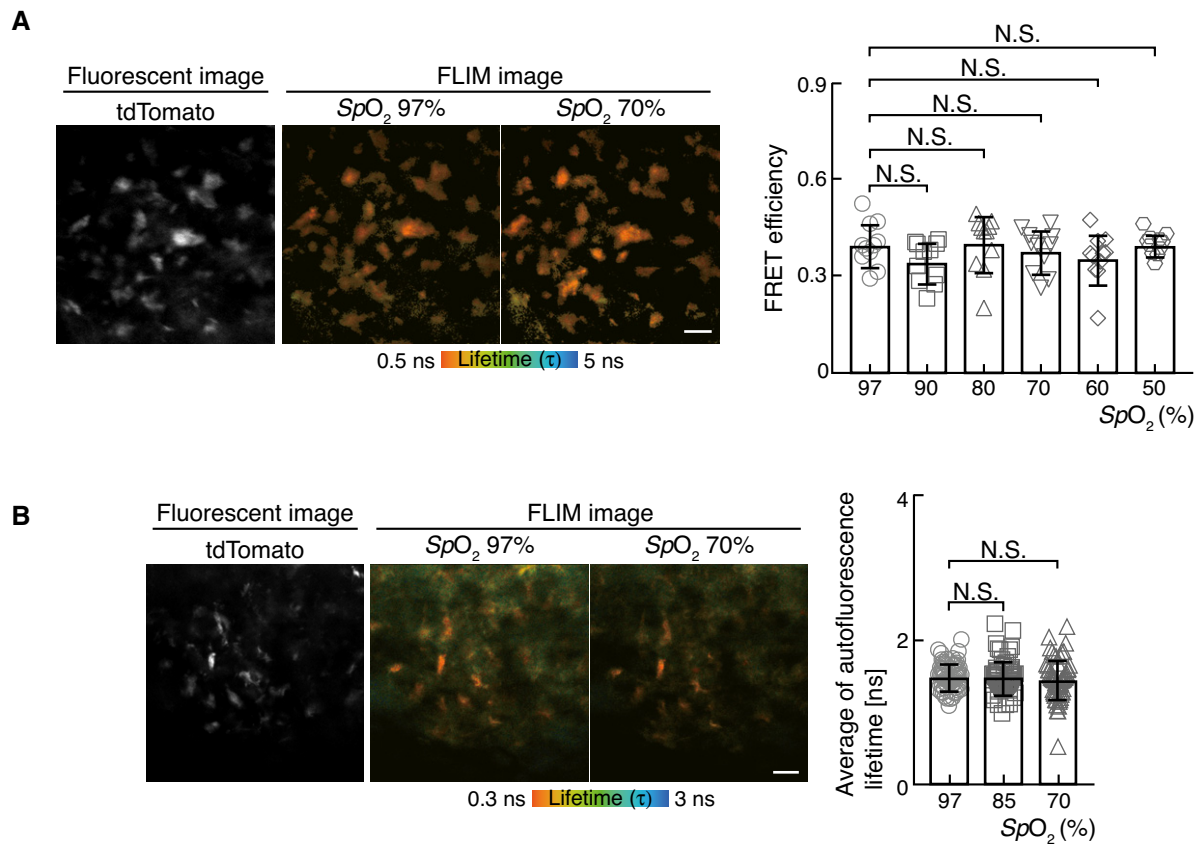
Figure 4. Effect of oxygen deprivation on energy metabolism *in vivo*.

A Representative intravital image of calvarial bone marrow of *Rosa26*^{GO-ATeam/+}; *Tg(Acp5-tdTomato)* male mice showing osteoclasts (left, tdTomato fluorescence) and FLIM image for ATP changes (middle and right, fluorescence lifetime of EGFP). The FRET efficiencies of each osteoclast were plotted from the mice upon exposure to low oxygen atmosphere (14% pO_2) or ambient air (right, $n = 11$ from three mice for each SpO_2). Scale bar, 20 μm. Data denote mean $\pm$ s.e.m. not significant (ANOVA).

B Representative intravital image of calvarial bone marrow of *Tg(Acp5-tdTomato)* male mice showing osteoclasts (left, tdTomato fluorescence) and NAD(P)H autofluorescence lifetime images (middle and right). Average of autofluorescence lifetime of each osteoclast was plotted from the mice upon exposure to low oxygen concentration (14% pO_2) or ambient air (right, $n = 64$ from three mice for each SpO_2). Scale bar, 20 μm. Data denote mean $\pm$ s.e.m. NS, not significant (ANOVA).

TETs play a pivotal role in oxygen sensing and are involved in osteoclastogenesis

To determine whether physiological hypoxia could affect cellular metabolic activities in osteoclasts, we assayed metabolites in osteoclast precursors using ion-chromatography (IC)-MS. The levels of TCA cycle metabolites, but not of glycolytic metabolites, were significantly changed in BMMs under 2% oxygen compared with those under 5% oxygen (Fig EV2A and B). In particular, 2-OG level in BMMs under 2% oxygen was significantly increased, predicting that physiological hypoxia may impair the activity of 2-OG-consuming enzyme. 2-OG-dependent dioxygenases catalyze hydroxylation reaction, which is inherently dependent on ambient oxygen tension, providing a molecular basis for the oxygen-sensing function of these enzymes. Physiological oxygen concentration in osteoclasts was found to be far below the Km values of PHDs for oxygen (Hirsila *et al*, 2003). Of the dioxygenases, TET and KDM proteins were highly expressed in both osteoclast precursors as well as mature osteoclasts (Figs EV3A–E, and EV4A and B, and Appendix Fig S2B) and

showed a high affinity for oxygen (Appendix Fig S3), allowing optimal hydroxylation reaction under the physiological oxygen levels in osteoclasts. Furthermore, the activity of an enzyme whose Km value for oxygen was ca. 40 μM was predicted to be dramatically decreased in mice during hypoxic air inhalation under physiological hypoxia (Appendix Fig S4). It was recently shown that some KDMs (KDM5A and 6A) directly modulate the methylation status of chromatin dependent on oxygen availability (Batie *et al*, 2019; Chakraborty *et al*, 2019). However, no obvious difference in methylation status of histone H3 was observed between 2% and 5% oxygen (Appendix Fig S5A). In contrast, since hypoxia induced DNA hypermethylation (Appendix Fig S5B), we hypothesized that TET proteins may serve as oxygen sensors in osteoclasts. In mammals, the TET protein family consists of three members, i.e., Tet1, Tet2, and Tet3. Although Tet2 has been found to be involved in the regulation of osteoclast differentiation, the role of Tet3 remains unclear (Chu *et al*, 2018). The role of Tet2 and Tet3 in osteoclasts was evaluated by generating osteoclast-specific *Tet2* and *Tet3* knockout mice by crossing *Tet2*^{flox/flox} and *Tet3*^{flox/flox} mice (Tanaka *et al*, 2020) with

$Rank^{Cre/+}$ mice to specifically disrupt *Tet2* and *Tet3* in osteoclast lineage cells ($Tet2_{Rank}^{-/-}$ and $Tet3a_{Rank}^{-/-}$, respectively). RANKL-induced formation of TRAP-positive MNCs in both $Tet2_{Rank}^{-/-}$ and $Tet3a_{Rank}^{-/-}$ BMMs was lower than that in wild-type BMMs (Fig 5 A). However, we observed no obvious bone phenotype in either $Tet2_{Rank}^{-/-}$ or $Tet3a_{Rank}^{-/-}$ mice (Figs 5B–D and EV5A). Although it has been previously reported that *Tet2* global knockout mice display high bone mass (Chu *et al*, 2018), this phenotype may have been caused by an abnormality in non-osteoclast lineage cells. Next, to explore the possibility that Tet3 may compensate for the loss of Tet2 and vice versa, we created osteoclast-specific *Tet2* and *Tet3* compound knockout mice ($Tet2_{Rank}^{-/-}$; $Tet3a_{Rank}^{+/-}$, $Tet2_{Rank}^{+/-}$; $Tet3a_{Rank}^{-/-}$ and $Tet2_{Rank}^{-/-}$; $Tet3a_{Rank}^{-/-}$, respectively). Bone volume of $Tet2_{Rank}^{-/-}$; $Tet3a_{Rank}^{+/-}$ and $Tet2_{Rank}^{+/-}$; $Tet3a_{Rank}^{-/-}$ mice was greatly enhanced (Fig 5B). Bone morphometric analysis revealed that osteoclast numbers as well as indicators of osteoclastic bone resorption in $Tet2_{Rank}^{-/-}$; $Tet3a_{Rank}^{+/-}$ and $Tet2_{Rank}^{+/-}$; $Tet3a_{Rank}^{-/-}$ mice were lower than those of wild-type control mice, whereas the parameters for bone formation in these mice were normal (Figs 5C and D, and EV5B–D). In addition, $Tet2_{Rank}^{-/-}$; $Tet3a_{Rank}^{-/-}$ mice exhibited an osteopetrotic phenotype characterized by an absence of osteoclasts, which was also observed in another type of osteoclast-specific *Tet2* and *Tet3* knockout mice generated by crossing $CX_3CR1^{Cre/+}$ mice (Appendix Fig S6). Consistent with these findings, deficiency in both *Tet2* and *Tet3* led to a decrease in RANKL-induced formation of TRAP-positive MNCs as well as the expression of osteoclast-related genes in a gene dose-dependent manner even under physioxia (Figs 5E and EV4C, and Appendix Fig S7A). In contrast, neither proliferative nor apoptotic activities of $Tet2_{Rank}^{-/-}$; $Tet3a_{Rank}^{+/-}$ BMMs were affected (Fig EV3D and E), similar to those of BMMs under 5% and 2% oxygen (Fig 1F and Appendix Fig S1C and D). In addition, overexpression of either of the Tet members tended to restore the impaired formation of TRAP-positive MNCs caused by a deficiency in both *Tet2* and *Tet3* (Appendix Fig S7B). These results collectively suggest that cooperation between Tet2 and Tet3 was important for osteoclast differentiation.

Next, to investigate the role of TET enzymes in osteoclastogenesis, we used a broad-spectrum inhibitor of 2-OG-dependent oxygenase (Hopkinson *et al*, 2013), IOX1, and a TET-specific inhibitor, octyl-2-hydroxyglutarate (2HG) (Figueroa *et al*, 2010). Treatment with IOX1 or 2HG impaired the formation of TRAP-positive MNCs as well as the expression of osteoclast-related genes (Appendix Fig S8A and B). Nevertheless, neither proliferative nor apoptotic

activities of BMMs were affected by IOX1 or 2HG (Appendix Fig S8C and D). Therefore, it is likely that the effects of 2HG and IOX1 are likely to mimic the effects of hypoxia (Fig 1F and Appendix Fig S1C and D). These findings, in turn, led to queries regarding the mechanism(s) underlying the regulation of osteoclast differentiation by TET enzymes. Tet2 and Tet3 catalyze active DNA demethylation and function as transcription regulators (Ito *et al*, 2010; Tsagaratou & Rao, 2013), which led us to assess the target(s) of Tet2- and Tet3-mediated regulation in osteoclastogenesis. To identify putative Tet2- and Tet3-regulated genes, we performed genome-wide screening of mRNA expression and methylated DNA regions in wild-type and $Tet2_{Rank}^{-/-}$; $Tet3a_{Rank}^{+/-}$ BMMs, following RANKL treatment. We initially selected gene loci that showed fewer methylation sites in wild-type cells than in $Tet2_{Rank}^{-/-}$; $Tet3a_{Rank}^{+/-}$ BMMs, following RANKL treatment, revealing that DNA methylation levels had been significantly changed in specific loci of 43 genes (Fig 6A; blue and red). We further selected the genes with significantly changed expression levels in $Tet2_{Rank}^{-/-}$; $Tet3a_{Rank}^{+/-}$ BMMs, compared with those of wild-type cells. This revealed that the expression levels of 25 genes, including osteoclast-related genes, were significantly decreased in $Tet2_{Rank}^{-/-}$; $Tet3a_{Rank}^{+/-}$ BMMs, where 6 genes were validated via quantitative RT–PCR and methylated DNA immunoprecipitation (MeDIP)-qPCR analysis (Fig 6A, red; Fig 6B and C, and Appendix Fig S9A and B). As Blimp1 (encoded by *Prdm1*) indirectly activates the master regulator of osteoclastogenesis, NFATc1, by downregulating anti-osteoclastogenic genes, such as *Bcl6* and *Mafb* (Kim *et al*, 2007; Miyauchi *et al*, 2010; Nishikawa *et al*, 2010), we hypothesized that a deficiency of Tet2 and Tet3 may disrupt the Blimp1-NFATc1 regulatory axis. Bisulfate sequencing showed that a region in the second intron of *Prdm1* was hypermethylated in $Tet2_{Rank}^{-/-}$; $Tet3a_{Rank}^{+/-}$ BMMs compared to that in the corresponding wild-type cells (Fig 6D and E). Furthermore, the expression of both *Prdm1* and *Nfatc1* in $Tet2_{Rank}^{-/-}$; $Tet3a_{Rank}^{+/-}$ BMMs was lower than that in the corresponding wild-type cells, while *Bcl6* and *Mafb* were highly expressed in $Tet2_{Rank}^{-/-}$; $Tet3a_{Rank}^{+/-}$ BMMs (Figs 6B and EV3C, and Appendix Fig S7A). In order to examine whether impaired osteoclastogenesis in $Tet2_{Rank}^{-/-}$; $Tet3a_{Rank}^{+/-}$ BMMs was caused by a loss of NFATc1 expression, we used a retroviral vector expressing NFATc1. Impaired osteoclast formation in $Tet2_{Rank}^{-/-}$; $Tet3a_{Rank}^{+/-}$ BMMs following RANKL treatment was significantly restored by NFATc1 overexpression (Fig 6F and Appendix Fig S9C). Furthermore, impaired osteoclast formation by IOX1 and 2HG was also restored by NFATc1 overexpression (Appendix Fig S9D). These

---

Figure 5. Osteoclast-specific *Tet2*- and *Tet3*-deficient mice exhibit a high bone mass phenotype.

A   Effect of *Tet2* and *Tet3* single deficiency on osteoclastogenesis. TRAP-stained cells (left panel) and the number of TRAP-positive cells with more than three nuclei (right). Scale bar, 100 μm. Data denote mean ± s.e.m. *$P < 0.05$; **$P < 0.01$ ($n = 6$ (control and $Tet2_{Rank}^{-/-}$) and $n = 3$ ($Tet3a_{Rank}^{-/-}$) biological replicates; ANOVA).

B   μCT analysis of the femurs of 10-week-old control ($n = 6$), $Tet2_{Rank}^{-/-}$ ($n = 5$), $Tet3_{Rank}^{-/-}$ ($n = 5$), $Tet2_{Rank}^{-/-}$; $Tet3a_{Rank}^{+/-}$ ($n = 6$), $Tet2_{Rank}^{+/-}$; $Tet3a_{Rank}^{-/-}$ ($n = 6$), and $Tet2_{Rank}^{-/-}$; $Tet3a_{Rank}^{-/-}$ ($n = 4$) male mice (axial view of the metaphyseal region). Scale, 0.5 mm.

C   Histological analysis of the proximal tibias of 10-week-old control, $Tet2_{Rank}^{-/-}$, $Tet3_{Rank}^{-/-}$, $Tet2_{Rank}^{-/-}$; $Tet3a_{Rank}^{+/-}$, $Tet2_{Rank}^{+/-}$; $Tet3a_{Rank}^{-/-}$ and $Tet2_{Rank}^{-/-}$; $Tet3a_{Rank}^{-/-}$ male mice (TRAP staining [red, osteoclasts]). Scale, 100 μm.

D   Parameters for osteoclastic bone resorption during bone morphometric analysis of 10-week-old control ($n = 10$), $Tet2_{Rank}^{-/-}$ ($n = 5$), $Tet3_{Rank}^{-/-}$ ($n = 6$), $Tet2_{Rank}^{-/-}$; $Tet3a_{Rank}^{+/-}$ ($n = 6$), $Tet2_{Rank}^{+/-}$; $Tet3a_{Rank}^{-/-}$ ($n = 6$) and $Tet2_{Rank}^{-/-}$; $Tet3a_{Rank}^{-/-}$ ($n = 4$) male mice. Data denote mean ± s.e.m. **$P < 0.01$; NS, not significant (ANOVA).

E   Effect of *Tet2* and *Tet3* double deficiency on osteoclastogenesis. TRAP-stained cells (left panel) and the number of TRAP-positive cells with more than three nuclei (right). Scale bar, 100 μm. Data denote mean ± s.e.m. **$P < 0.01$ ($n = 6$ (control), $n = 10$ ($Tet2_{Rank}^{-/-}$; $Tet3a_{Rank}^{+/-}$), $n = 3$ ($Tet2_{Rank}^{+/-}$; $Tet3a_{Rank}^{-/-}$), and $n = 4$ ($Tet2_{Rank}^{-/-}$; $Tet3a_{Rank}^{-/-}$) biological replicates; ANOVA).
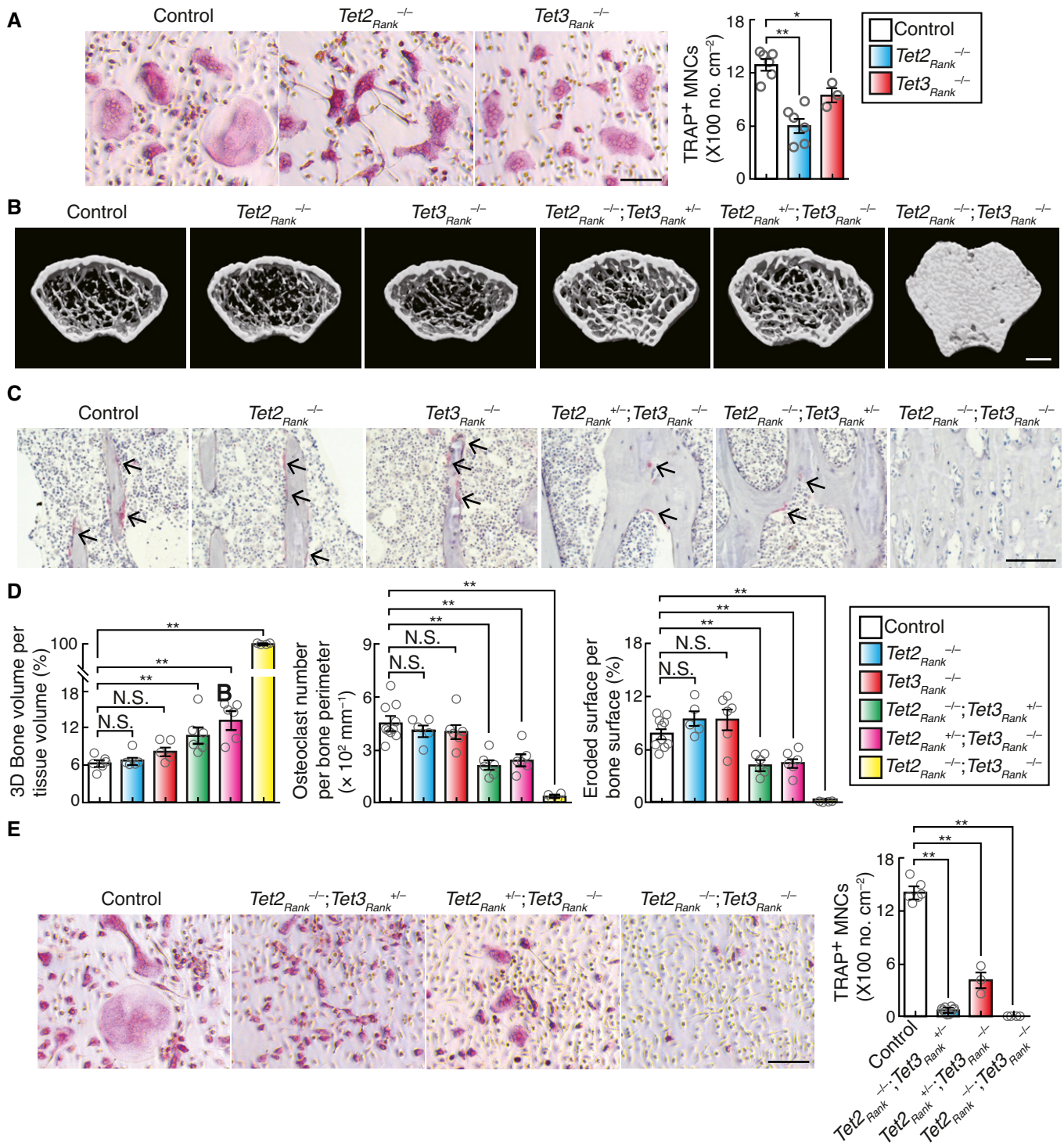
Figure 5.

results suggested that the Blimp1-NFATc1 axis was a crucial step for Tet2- and Tet3-mediated osteoclast regulation.

In order to determine whether Tet2- and Tet3-mediated DNA demethylation is affected by physiological hypoxia and serves as an oxygen sensor in osteoclasts, we investigated DNA methylation levels at the *Prdm1* locus in osteoclasts, under conditions of

physioxia and physiological hypoxia. A significant difference in DNA methylation was observed between 5% and 2% oxygen, suggesting that Tet2- and Tet3-mediated DNA demethylation was severely impaired by physiological hypoxia (Fig 6G). Furthermore, the expression of both *Prdm1* and *Nfatc1* under 2% oxygen was lower than that under 5% oxygen, while that of *Bcl6* and *Mafb* was

high (Fig 3A and C). NFATc1 overexpression restored osteoclast formation even under 2% oxygen (Fig 6H and Appendix Fig S9E). However, since the extent of the recovery was low, it is conceivable that physiological hypoxia may inhibit osteoclastogenesis by reducing the activity of other oxygen-dependent dioxygenases as well as TETs. Taken together, these results suggested that the Tet2- and Tet3-mediated Blimp1–NFATc1 axis was crucial step in osteoclastic adaptation to physioxia perturbation.

Discussion

The oxygen tension of the endosteal region wherein the osteoclasts reside was previously determined to be 13.5 mmHg outside the vessels and 21.9 mmHg inside the vessels (Spencer *et al*, 2014). The widely used 2PLIM method with a cell-impermeable phosphorescent probe enables the measurement of only extracellular oxygen tension. However, oxygen is mainly stored intracellularly through the function of oxygen storage proteins such as hemoglobin, myoglobin, cytoglobin, and neuroglobin, whereas the dissolved oxygen level in the extracellular fluid is reduced in accordance with Henry's law. Therefore, the previous method may underestimate the actual cellular oxygen tension *in vivo*. Here, using an updated 2PLIM method with our newly developed cell-penetrating phosphorescent probe, we succeeded in determining the physiological range of oxygen tension in the bone marrow at the single-cell resolution, revealing that the precise oxygen tension experienced by osteoclasts *in vivo* ranged from 17.4 to 36.4 mmHg. We further demonstrated that energy metabolism in osteoclasts remains unaffected within the physiological range of oxygen tension *in vivo*. Although cytochrome c oxidase is one of the key enzymes for the respiratory function of mitochondria, the K_M for oxygen of cytochrome c oxidase is extremely low (< 0.77 mmHg) (Krab *et al*, 2011). Therefore, energy metabolism is likely to provide robustness to osteoclasts against hypoxia, at least under both physioxia and physiological hypoxia conditions.

We demonstrated that HIF-α is induced in osteoclasts and activates the expression of hypoxia-related genes, but is not dispensable for osteoclastogenesis under both physioxia and physiological hypoxia conditions. Considering that PHDs have a high K_M for oxygen, ranging from 87 to 299 mmHg (Wilson *et al*, 2020), it seems that the HIF–PHD axis is constitutively activated in osteoclasts even under physioxia, and may not be directly involved in mediating the hypoxia response. In contrast, oxygen tension in the cortical tubules of the kidney has been estimated to be 60 mmHg in live mice under conditions of room air inhalation and to be 35 mmHg under conditions of 15% oxygen inhalation (Hirakawa *et al*, 2015), which is a markedly higher level than that determined in osteoclasts. It is thus reasonable to speculate that PHDs act as key regulators for oxygen sensing and are involved in the regulation of HIF-target genes such as *Epo* under changing oxygen conditions *in vivo*.

Accumulating evidence shows that dioxygenase family members with different affinities for oxygen could be potential oxygen sensors. Indeed, KDM5A- or KDM6A-mediated histone demethylation is severely inhibited by hypoxia, with implications for tumorigenesis (Batie *et al*, 2019; Chakraborty *et al*, 2019). However, given their extremely high K_M values for oxygen (117 and 260 mmHg, respectively), histone hypermethylation in osteoclasts is likely to be significantly promoted. This may explain why we did not observe an effect of physioxia or physiological hypoxia on the histone methylation status of osteoclasts in this study. Alternatively, we demonstrated that TETs play a pivotal oxygen-sensing role in osteoclasts. Considering TETs with a K_M of 39 mmHg (Laukka *et al*, 2016), the enzymatic activity of TETs could be markedly attenuated by changing the oxygen tension from 36.9 to 17.4 mmHg. Thus, our findings provide a rational molecular basis for the hypoxia response within the physiological range of oxygen tension *in vivo*.

Although the effect of hypoxia on osteoclast differentiation has been extensively studied to date (Arnett *et al*, 2003; Fukuoka *et al*, 2005; Murata *et al*, 2017), the conclusion of our analysis was contrary to the conclusion reported in a few previous studies, namely, that oxygen acts as a positive regulator for osteoclast differentiation. The previous studies showed that osteoclast differentiation was promoted by a decrease in oxygen tension in

---

Figure 6. Tet2- and Tet3-mediated DNA demethylation is required for the activation of Blimp1-NFATc1 axis.

A   Scatter plot of fold changes in RNA-seq data and MeDIP-seq data. The $\log_2$ fold changes in RNA-seq expression between wild-type control and $Tet2_{Rank}{}^{-/-}$; $Tet3a_{Rank}{}^{+/-}$ BMMs stimulated with RANKL for 2 days are shown on the x-axis, and $\log_2$ fold changes in MeDIP-seq expression (> 0) are shown on the y-axis. The names of significant genes are labeled (FDR of differential expression analysis < 0.01, p-value of differential methylated region analysis < 0.01).

B   MeDIP-qPCR analysis to validate regions that are hypermethylated in $Tet2_{Rank}{}^{-/-}$; $Tet3a_{Rank}{}^{+/-}$ BMMs stimulated with RANKL for 2 days. Data denote mean ± s.e.m. *P < 0.05; **P < 0.01 (n = 3–5 biological replicates; t-test).

C   Gene expression of TET target candidates in BMMs stimulated with RANKL for 2 days. Data denote mean ± s.e.m. **P < 0.01 (n = 4–7 biological replicates; t-test).

D   Genome browser view of the expression and the methylation site distribution in the *Prdm1* gene locus of control and $Tet2_{Rank}{}^{-/-}$; $Tet3a_{Rank}{}^{+/-}$ BMMs stimulated with RANKL for 2 days.

E   Bisulfate sequencing analysis of selected region of the second intron of the *Prdm1* gene in control and $Tet2_{Rank}{}^{-/-}$; $Tet3a_{Rank}{}^{+/-}$ BMMs stimulated with RANKL for 2 days.

F   Effect of retroviral NFATc1 expression on osteoclastogenesis of control and $Tet2_{Rank}{}^{-/-}$; $Tet3a_{Rank}{}^{+/-}$ BMMs stimulated with RANKL for 3 days. TRAP-stained cells (left panel) and the number of TRAP-positive cells with more than three nuclei (right). Scale bars, 100 μm. Data denote mean ± s.e.m. **P < 0.01 (n = 3 biological replicates; ANOVA).

G   Bisulfate sequencing analysis of the selected region of the second intron of the *Prdm1* gene in BMMs stimulated with RANKL and culture under 5% and 2% oxygen for 3 days.

H   Effect of retroviral NFATc1 expression on osteoclastogenesis of BMMs stimulated with RANKL and culture under 5% and 2% oxygen for 5 days. Control and $Tet2_{Rank}{}^{-/-}$; $Tet3a_{Rank}{}^{+/-}$ BMMs stimulated with RANKL for 3 days. TRAP-stained cells (left panel) and the number of TRAP-positive cells with more than three nuclei (right). Scale bars, 100 μm. Data denote mean ± s.e.m. **P < 0.01 (n = 3 biological replicates; ANOVA).
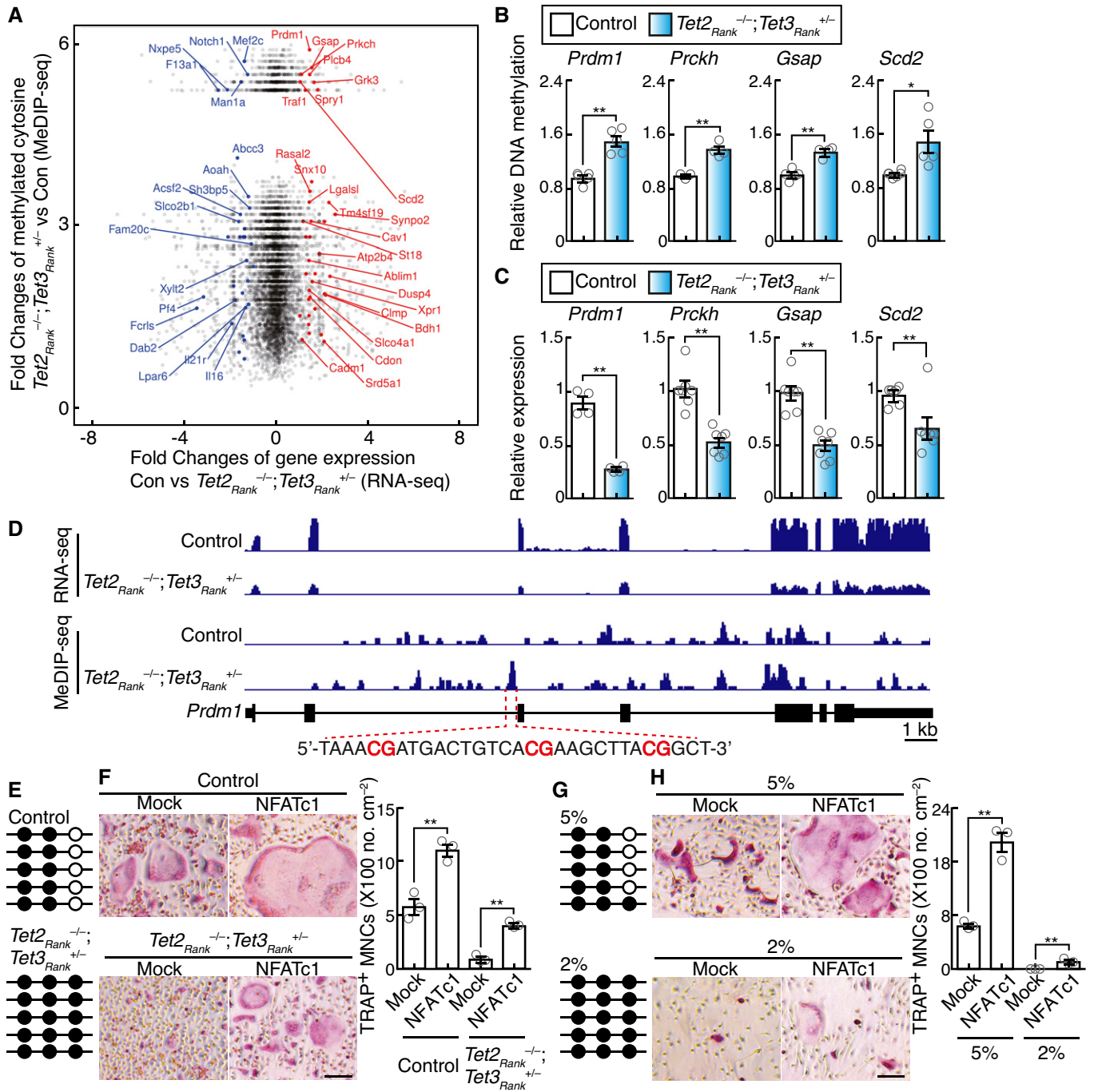
Figure 6.

comparison with that in room air condition (18% oxygen as a control). Since such cell culture experiments are performed under supra-physiological oxygen tension, these results may be misleading, which could be the main cause of discrepancy between the previous data and our present *in vivo/in vitro* results. Although routine cell culture in room air is one of the mainstays of life science research, primary cell-based *in vitro* analysis under physioxia condition may have made our experiments more robust and increased the likelihood that these findings have *in vivo* relevance.

Materials and Methods

Mice and bone analysis

We generated and genotyped *Tet2*[flox/flox], *Tet3*[flox/flox], *Hif1*[flox/flox], *Hif2*[flox/flox], *RANK*[Cre/+], *CX$_3$CR1*[Cre/+], *Tg(Acp5-tdTomato)*, *Epo*^{−/−};*Tg (3.3K-Epo)*, *Tcirg*[GFP/+], and *Rosa26*[GO-ATeam2/+] mice as previously described (Sun-Wada *et al*, 2009; Maeda *et al*, 2012; Kikuta *et al*, 2013; Yamazaki *et al*, 2013; Yona *et al*, 2013; Semba *et al*, 2016; Yamamoto *et al*, 2019; Tanaka *et al*, 2020). *Hif1*^{+/+};*Hif2*^{+/+},

Hif1$^{flox\ or\ +/flox\ or\ +}$;Hif2$^{flox\ or\ +/flox\ or\ +}$, Tet2$^{+/+}$;Tet3$^{+/+}$ and *Tet2$^{flox\ or\ +/flox\ or\ +}$;Tet3$^{flox\ or\ +/flox\ or\ +}$* littermate mice that did not carry the Cre recombinase were used as control (referred to as control, wild-type, or wild-type control). There are no differences in bone phenotype among them. All mice were born and maintained under specific pathogen-free conditions, and all animal studies were approved by the Institutional Animal Care and Use Committee of both Doshisha University and Osaka University. All strains were on the C57BL/6 background. Ten-week-old sex-matched mice were used for experiments unless otherwise mentioned. Animals were randomly included in the experiments according to genotyping results. Animal experiments were conducted in a blinded fashion with respect to the investigator. The numbers of animals used per experiment are stated in the figure legends. Three-dimensional microcomputed tomography (µCT) analyses and bone morphometric analyses were performed as described previously (Nishikawa *et al*, 2015; Baba *et al*, 2018; Suzuki *et al*, 2020).

To investigate acute hypoxic effect *in vivo,* we attempted to examine the *in vivo* effect of hypoxia using the mice under 10% or less oxygen concentration; however as the mice were exposed to these conditions for 10 days, they did not consume food and displayed hypoactivity and lean mass with less bone mass. Therefore, we exposed the mice to 14% oxygen concentration. Oxygen was diluted with more than 97% nitrogen generated by N$_2$ generator (TAITEC) using rotameters to deliver a hypoxic gas mixture into the breathing chamber (Natsume). The oxygen concentration was continuously monitored inside the chamber using gas analyzer (Astec). All of the mice were killed and subjected to µCT and bone morphometric analyses 10 days after exposure.

Two-photon phosphorescence lifetime and fluorescence lifetime imaging

Intravital microscopy of mouse calvaria bone tissues was performed as described previously (Morimoto *et al*, 2021). Ten- to sixteen-week-old mice were anesthetized with isoflurane, the frontoparietal regions of the skull bones were exposed, and then, the internal surfaces of bones adjacent to bone marrow cavity were observed by using two-photon excitation microscopy. The imaging systems consisted of an upright two-photon microscope (FVMPE-RS, Olympus) equipped with a × 25 water-immersion objective (XLPLN 25XWMP2, N.A. 1.05; Olympus) driven by laser (Mai Tai DeepSee, Ti:Sapphire; Spectra-Physics) tuned to 750–850 nm. An acousto-optic modulator (AOM) was placed in the excitation path of two-photon microscope, enabling fast repetitive on–off switching of the laser excitation. For phosphorescence measurement, the mice were intravenously injected with 8.4 mg/kg BTPDM1 (Yoshihara *et al*, 2015) before imaging. It has been previously demonstrated that BTPDM1 distributes to most tissues in the body within 2 h after injection and accumulates in the cells of these tissues for at least 24 h. Furthermore, phosphorescence imaging using BTPDM1 determined that oxygen level in hypoxic tumors, renal cortex, and hepatic lobules in live animals ranged from 0.8 to 60 mmHg (Hirakawa *et al*, 2015; Yoshihara *et al*, 2015; Mizukami *et al*, 2020), showing that BTPDM1 has high sensitivity with a wide dynamic range. Phosphorescent and fluorescent and images were collected at a depth of 100–150 µm below the skull bone surface and detected through band-pass emission filters at 450/50 nm (for NAD(P)H

autofluorescence), 525/50 nm (for GFP and EGFP), and 620/60 nm (for tdTomato and BTPDM1). To perform inhalation exposure of mice to low oxygen, oxygen was diluted with more than 97% nitrogen using rotameters (KOFLOC) to deliver gas mixtures, from 21 to 14% oxygen, into the breathing apparatus. To monitor the degree of hypoxia *in vivo*, a probe attached to the thigh of the mice was used to measure the heart rate, peripheral oxygen saturation (SpO_2), and breath rate using MOUSEOX PLUS (STARR LifeSciences).

Phosphorescence lifetime imaging microscopy (PLIM) and fluorescence lifetime imaging microscopy (FLIM) images were acquired by TCSPC method using DCS-120 confocal scanning system (Becker & Hickl GmbH/Tokyo Instruments). Single-photon emission signals were collected through emission filters (450/50 nm for NAD(P)H autofluorescence, 525/50 nm for EGFP of GO-ATeam2, and 620/60 nm for BTPDM1). SPCImage software (Becker & Hickl GmbH) was used to fit the signal of each pixel to a single-exponential decay for the phosphorescence of BTPDM1, a double-exponential decay for the fluorescence of EGFP, and a triple-exponential decay for the autofluorescence of NAD(P)H according to the following equations:

$$N(x,\ y,\ t) = A_1(x,\ y)e^{-t/\tau_1(x,y)} \tag{1}$$

$$N(x,\ y,\ t) = A_1(x,\ y)e^{-t/\tau_1(x,y)} + A_2(x,\ y)e^{-t/\tau_2(x,y)} \tag{2}$$

$$N(x,\ y,\ t) = A_1(x,\ y)e^{-t/\tau_1(x,y)} + A_2(x,\ y)e^{-t/\tau_2(x,y)} + A_3(x,\ y)e^{-t/\tau_3(x,y)} \tag{3}$$

where x and y are the pixel coordinates, N is the measured counts, A is the amplitude, and t is the lifetime. Chi-square contains the squared difference between all measured data points and the modeled decay, each of which is weighted according to the expected standard deviation of the measured intensity and (for the reduced chi-square) the total number of data points:

$$\chi^2 = \left[\sum_{i=1}^{n} \frac{(N(t_i) - N_c(t_i))^2}{N(t_i)} \right] \times \frac{1}{n} \tag{4}$$

Here, $N(t_k)$ is the measured counts at time t_k, $N_c(t_k)$ is the modeled number of counts at time t_k, and n is the number of data points. A good fit was characterized by a value of chi-square close to 1 (at least, less than 1.34). We extracted both best-fit amplitudes and lifetimes from the region of interests (ROIs) corresponding to osteoclasts. The average lifetime for each ROIs can then be calculated using the following equations:

$$\tau_{\mathrm{avg}} = \frac{\sum\limits_{i=1}^{n} A_i \tau_i^2}{\sum\limits_{i=1}^{n} A_i \tau} \tag{5}$$

where n is 0, 1, and 2 for a single-exponential, a double-exponential, and a triple-exponential decay, respectively.

The FRET efficiency of GO-ATeam2 is defined as the proportion of the donor protein, EGFP, that have transferred excitation state energy to the acceptor protein, OFP. It can be expressed in terms of measurable quantities as $1 - \tau_{\mathrm{FRET}}/\tau_d$. τ_d is the amplitude-weighted average lifetime of the donor.

For *in vitro* analysis to generate a calibration curve of phosphorescence lifetime vs. oxygen tension, BMMs stimulated with RANKL for 2 days were treated with 10 μM BTPDM1 and then were observed by using two-photon excitation microscopy equipped with cell culture incubator (Stage top incubator, Tokai Hit). While diluting oxygen concentration in the culture media with more than 97% nitrogen using rotameters (KOFLOC), phosphorescent images were collected through band-pass emission filters at 620/60 nm (BTPDM1) at each concentration of oxygen in the culture media (from 6 to 0% oxygen, which was monitored using Microx 4 [TAITEC]). PLIM images were acquired by TCSPC method using DCS-120 confocal scanning system (Becker & Hickl GmbH/Tokyo Instruments). Single-photon emission signals were collected through emission filters (620/60 nm). SPCImage software (Becker & Hickl GmbH) was used to fit the signal of each pixel to a single-exponential decay according to the equation (1). The phosphorescence quenching due to dissolved oxygen in solution can be examined by the following Stern–Volmer equation:

$$\frac{1}{\tau_p} = \frac{1}{\tau_p^0} + k_q p O_2 \tag{6}$$

in which τ_p is the phosphorescence lifetime and k_q is a bimolecular quenching rate constant.

Cell culture

In vitro osteoclast differentiation was described previously (Nishikawa *et al*, 2010, 2013, 2015). Briefly, for *in vitro* differentiation, bone marrow-derived cells cultured with 10 ng/ml M-CSF (Miltenyi Biotec) for 2 days were used as osteoclast precursor cells and bone marrow-derived monocyte/macrophage precursor cells (BMMs) and were further cultured with 50 ng/ml RANKL (PeproTech) in the presence of 10 ng/ml M-CSF for 3 days. Tartrate-resistant acid phosphatase (TRAP)-positive multinucleated cells (MNCs; TRAP+MNCs, more than three nuclei) were counted. Exposure of cell cultures to physioxia (5% oxygen) and physiological hypoxia (2% oxygen) was undertaken in the hypoxia workstation *IN VIVO* 300 (Ruskinn) and multi-gas incubator (Astec).

Quantitative RT–PCR analysis

Quantitative RT–PCR analysis was performed as described previously (Sakaguchi *et al*, 2018). Briefly, total RNA and cDNA were prepared using the RNeasy Mini Kit (Qiagen) and Superscript III reverse transcriptase (Invitrogen), respectively, according to the manufacturer's instructions. Real-time PCR was performed with a Thermal Cycler Dice Real Time System (TaKaRa Bio) using SYBR Premix EX Taq (TaKaRa Bio). The primer sequences are listed in Appendix Table S1.

Transcriptome analysis

For RNA-seq analysis, library preparation was performed using a TruSeq Stranded mRNA Sample Prep Kit (Illumina, San Diego, CA) according to the manufacturer's instructions. Sequencing was performed on an Illumina HiSeq 2500 platform in a 75-base single-end mode. Illumina Casava1.8.2 software was used for basecalling.

Sequenced reads were mapped to the mouse reference genome sequences (mm10) using TopHat v2.0.13 in combination with Bowtie2 ver. 2.2.3 and SAMtools ver. 0.1.19. Gene expression quantification was performed by htseq-count (Anders *et al*, 2015). Differential expression analysis was performed using the Bioconductor package, edgeR (Robinson *et al*, 2010).

GeneChip analysis was performed as described previously (Nishikawa *et al*, 2010). Briefly, total RNA was converted into cDNA by reverse transcription. Biotinylated cRNA was then synthesized by *in vitro* transcription. After cRNA fragmentation, hybridization with the mouse genome 430 2.0 array (Affymetrix) was performed. The core data set has been deposited in the Genome Network Platform (http://genomenetwork.nig.ac.jp/).

Metabolome analyses by ion-chromatography mass spectrometry

Metabolites of central metabolic pathways were extracted from the cultured cells for metabolome analyses as described previously (Semba *et al*, 2016). Briefly, the cells were scraped with methanol containing an internal standard, followed by the addition of chloroform and ultrapure water (Wako) to the aqueous phase to obtain the extracted hydrophilic metabolites. The aqueous phase was subjected to centrifugal filtration through a 5-kDa-cutoff filter tube (Human Metabolome Technologies), concentrated in a vacuum concentrator, and then dissolved in ultrapure water for IC-MS analysis (Hu *et al*, 2015). For metabolome analysis, metabolites were measured using an Orbitrap-type MS (Q-Exactive Focus; Thermo Fisher Scientific) connected to a high-performance IC system (ICS-5000+, Thermo Fisher Scientific), as previously described (Semba *et al*, 2016; Okuno *et al*, 2020).

DNA methylation analysis

We prepared genomic DNA from cultured cells using the GenElute Mammalian Genomic DNA Miniprep Kit (Sigma-Aldrich) according to the manufacturer's instructions. For bisulfate genomic sequencing, genomic DNA was subjected to bisulfate conversion with the EpiTect Bisulfate Kit (Qiagen). Following bisulfate PCR, the products were cloned into the pGEM-T Easy vector (Promega) and subjected to sequencing. The primer sequences are listed in Appendix Table S1.

Before carrying out methylated DNA immunoprecipitation (MeDIP)-seq and MeDIP-quantitative PCR (qPCR) analysis, we sonicated genomic DNA to produce random fragments ranging in size up to 150 bp using DNA shearing system (Covaris). Methylated DNA was enriched from the fragmented genomic DNA using the MEDIP Kit (Active Motif). For MeDIP-seq analysis, the Illumina libraries were prepared using KAPA Hyper Prep Kit (Kapa Biosystems) and TruSeq DNA UD Indexes (Illumina) according to manufacturer's instructions. Paired-end sequencing (100 bp × 2) was performed using HiSeq3000 (Illumina). Sequenced reads were trimmed with Trim Galore and mapped to the mouse genome (mm10) with Bowtie2 (Langmead & Salzberg, 2012). For the analysis of differentially methylated regions, peak calling and significance tests were performed with the R/Bioconductor package MEDIPS (Lienhard *et al*, 2014). BedGraph and BigWig files were generated and viewed using the UCSC Genome Browser.

For MeDIP-qPCR analysis, we carried out real-time PCRs with input DNA and the immunoprecipitated methylated DNA using SYBR Premix EX Taq (TaKaRa Bio). To evaluate the relative

enrichment of target sequences after MeDIP-qPCR, we calculated the ratios of the signals for immunoprecipitated DNA versus input DNA. The primer sequences are listed in Appendix Table S1.

Gene transfer

The retroviral vector pMX-NFATc1-IRES-GFP was constructed by inserting DNA fragments encoding NFATc1 into pMX-IRES-GFP (Morita *et al*, 2000). Retroviral packaging was performed by transfecting the plasmids into Plat-E cells using FuGENE6 as described previously (Morita *et al*, 2000). Ten hours after inoculation with retroviruses, BMMs were stimulated with RANKL.

RNA transfection experiment was performed as described previously (Nishikawa & Ishii, 2021). Briefly, synthetic capped RNA was made with the mMESSAGE mMACHINE T7 ULTRA Transcription Kit (Thermo) using linearized DNA of the pcDNA3-TET derivatives and then purified by RNeasy Mini Kit (Qiagen). RNA transfections were performed with the Lipofectamine MessengerMAX (Thermo). Two hours after transfection with RNA, BMMs were stimulated with RANKL.

Immunoblot analysis

Cell lysates were subjected to immunoblot analysis using antibodies specific for Tet1 (Active Motif, 614444), Tet2 (Abcam, ab124297), Tet3 (GeneTex, GTX121453), Blimp1 (Novus, NB600-235), NFATc1 (Santa Cruz Biotechnology, sc-7294), TRAP (Santa Cruz Biotechnology, sc-30833), Ctsk (Daiichi Finechemical, F-95), HIF-1α (CST, #36169), HIF-2α (Abcam, ab199), H3K9me3 (FUJIFILM, MABI0308), H3K27me3 (FUJIFILM, MABI0323), H3K36me3 (FUJIFILM, MABI0333), H3 (CST, #4499), 5mC (Active Motif, 39649), and Lmnb (Santa Cruz Biotechnology, sc-6217). Whole-cell extracts were prepared by lysis in radioimmunoprecipitation assay (RIPA) buffer (Iwamoto *et al*, 2016).

Flow cytometry analysis

Single-cell suspensions were incubated with anti-CD16/CD32 for 10 min and then stained with phycoerythrin-conjugated anti-CD11b (M1/70; eBioscience) in flow cytometry (FACS) buffer (1× phosphate-buffered saline [PBS], 4% heat-inactivated fetal calf serum, and 2 mM EDTA) for 15 min.

For BrdU detection, CD11b-stained cells were fixed and permeabilized with Cytofix/Cytoperm solution (BD Biosciences) for 15 min and then washed with 1×Perm/Wash buffer (BD Biosciences). The cells were further permeabilized in Cytoperm plus buffer (BD Biosciences) for 10 min and then washed with 1×Perm/Wash buffer. The washed cells were resuspended in Cytofix/Cytoperm solution for 5 min and then washed with 1XPerm/Wash buffer; they were treated with DNase I and incubated at 37°C for 1 h and then washed aging with 1×Perm/Wash buffer. The cells were then stained with fluorescein isothiocyanate-conjugated anti-BrdU (3D4; BioLegend) for 15 min.

For Annexin V detection, CD11b-stained cells were stained with allophycocyanin-conjugated anti-Annexin V (BD Biosciences) in 1×Annexin V binding buffer (BD Biosciences) for 20 min.

The stained cells were analyzed on a CytoFLEX (Beckman Coulter). FACS data were statistically analyzed with FlowJo software (BD Biosciences).

Statistical analysis

All data are expressed as mean ± s.e.m. Statistical analysis was performed using the unpaired two-tailed Student's *t*-test for comparisons between two groups and analysis of variance with the Bonferroni *post hoc* test for comparisons among three or more groups (*$P < 0.05$; **$P < 0.01$; NS, not significant, throughout the paper). All data met the assumption of statistical tests and had a normal distribution, and variance was similar between groups that were statistically compared. Replicates used were biological replicates. The results are representative examples of more than three independent experiments. We estimated the sample size considering the variation and mean of the samples. We tried to reach the conclusion using as small a size of samples as possible. We usually excluded samples if we observed any abnormality in terms of size, weight, or apparent disease symptoms in mice before performing experiments. However, we did not exclude animals here, as we did not observe any abnormalities in the present study.

Data availability

The RNA-seq and MBD-seq data have been deposited in the Gene Expression Omnibus database (accession code GSE156130 [https://www.ncbi.nlm.nih.gov/geo/query/acc.cgi?acc = GSE156130]). GeneChip data have been deposited in the Genome Network Platform (http://genomenetwork.nig.ac.jp/).

Expanded View for this article is available online.

Author contributions

KN conceptualized the study; KN, TY, AN, JK, YS, RS, MS, ST, YM, MI investigated the study; SS, DO, DM, and HM involved in formal analysis; NS, NT, HS, MY, YK, HK, and MY contributed to methodology; KN wrote—original draft.

Conflict of interest

The authors declare that they have no conflict interest.

References

Anders S, Pyl PT, Huber W (2015) HTSeq–a Python framework to work with high-throughput sequencing data. *Bioinformatics* 31: 166–169

Arnett TR, Gibbons DC, Utting JC, Orriss IR, Hoebertz A, Rosendaal M, Meghji S (2003) Hypoxia is a major stimulator of osteoclast formation and bone resorption. *J Cell Physiol* 196: 2–8

Baba M, Endoh M, Ma W, Toyama H, Hirayama A, Nishikawa K, Takubo K, Hano H, Hasumi H, Umemoto T *et al* (2018) Folliculin regulates osteoclastogenesis through metabolic regulation. *J Bone Miner Res* 33: 1785–1798

Batie M, Frost J, Frost M, Wilson JW, Schofield P, Rocha S (2019) Hypoxia induces rapid changes to histone methylation and reprograms chromatin. *Science* 363: 1222–1226

Boyle WJ, Simonet WS, Lacey DL (2003) Osteoclast differentiation and activation. *Nature* 423: 337–342

Chakraborty AA, Laukka T, Myllykoski M, Ringel AE, Booker MA, Tolstorukov MY, Meng YJ, Meier SR, Jennings RB, Creech AL *et al* (2019) Histone demethylase KDM6A directly senses oxygen to control chromatin and cell fate. *Science* 363: 1217–1222

Chu Y, Zhao Z, Sant DW, Zhu G, Greenblatt SM, Liu L, Wang J, Cao Z, Tho JC, Chen S *et al* (2018) Tet2 regulates osteoclast differentiation by interacting with Runx1 and maintaining genomic 5-Hydroxymethylcytosine (5hmC). *Genomics Proteomics Bioinformatics* 16: 172–186

Dirckx N, Tower RJ, Mercken EM, Vangoitsenhoven R, Moreau-Triby C, Breugelmans T, Nefyodova E, Cardoen R, Mathieu C, Van der Schueren B *et al* (2018) Vhl deletion in osteoblasts boosts cellular glycolysis and improves global glucose metabolism. *J Clin Invest* 128: 1087–1105

Figueroa ME, Abdel-Wahab O, Lu C, Ward PS, Patel J, Shih A, Li Y, Bhagwat N, Vasanthakumar A, Fernandez HF *et al* (2010) Leukemic IDH1 and IDH2 mutations result in a hypermethylation phenotype, disrupt TET2 function, and impair hematopoietic differentiation. *Cancer Cell* 18: 553–567

Fukuoka H, Aoyama M, Miyazawa K, Asai K, Goto S (2005) Hypoxic stress enhances osteoclast differentiation via increasing IGF2 production by non-osteoclastic cells. *Biochem Biophys Res Commun* 328: 885–894

Guntur AR, Le PT, Farber CR, Rosen CJ (2014) Bioenergetics during calvarial osteoblast differentiation reflect strain differences in bone mass. *Endocrinology* 155: 1589–1595

Hammarlund EU, Flashman E, Mohlin S, Licausi F (2020) Oxygen-sensing mechanisms across eukaryotic kingdoms and their roles in complex multicellularity. *Science* 370: eaba3512

Hayashi M, Nakashima T, Taniguchi M, Kodama T, Kumanogoh A, Takayanagi H (2012) Osteoprotection by semaphorin 3A. *Nature* 485: 69–74

Hirakawa Y, Yoshihara T, Kamiya M, Mimura I, Fujikura D, Masuda T, Kikuchi R, Takahashi I, Urano Y, Tobita S *et al* (2015) Quantitating intracellular oxygen tension *in vivo* by phosphorescence lifetime measurement. *Sci Rep* 5: 17838

Hirsila M, Koivunen P, Gunzler V, Kivirikko KI, Myllyharju J (2003) Characterization of the human prolyl 4-hydroxylases that modify the hypoxia-inducible factor. *J Biol Chem* 278: 30772–30780

Hopkinson RJ, Tumber A, Yapp C, Chowdhury R, Aik W, Che KH, Li XS, Kristensen JBL, King ONF, Chan MC *et al* (2013) 5-Carboxy-8-hydroxyquinoline is a broad spectrum 2-oxoglutarate oxygenase inhibitor which causes iron translocation. *Chem Sci* 4: 3110–3117

Hu S, Wang J, Ji EH, Christison T, Lopez L, Huang Y (2015) Targeted metabolomic analysis of head and neck cancer cells using high performance ion chromatography coupled with a Q exactive HF mass spectrometer. *Anal Chem* 87: 6371–6379

Ishii KA, Fumoto T, Iwai K, Takeshita S, Ito M, Shimohata N, Aburatani H, Taketani S, Lelliott CJ, Vidal-Puig A *et al* (2009) Coordination of PGC-1beta and iron uptake in mitochondrial biogenesis and osteoclast activation. *Nat Med* 15: 259–266

Ito S, D'Alessio AC, Taranova OV, Hong K, Sowers LC, Zhang Y (2010) Role of Tet proteins in 5mC to 5hmC conversion, ES-cell self-renewal and inner cell mass specification. *Nature* 466: 1129–1133

Iwamoto Y, Nishikawa K, Imai R, Furuya M, Uenaka M, Ohta Y, Morihana T, Itoi-Ochi S, Penninger JM, Katayama I *et al* (2016) Intercellular communication between keratinocytes and fibroblasts induces local osteoclast differentiation: a Mechanism underlying cholesteatoma-induced bone destruction. *Mol Cell Biol* 36: 1610–1620

Jaakkola P, Mole DR, Tian Y-M, Wilson MI, Gielbert J, Gaskell SJ, Kriegsheim AV, Hebestreit HF, Mukherji M, Schofield CJ *et al* (2001) Targeting of HIF-alpha to the von Hippel-Lindau ubiquitylation complex by O2-regulated prolyl hydroxylation. *Science* 292: 468–472

Kalinina S, Breymayer J, Schafer P, Calzia E, Shcheslavskiy V, Becker W, Ruck A (2016) Correlative NAD(P)H-FLIM and oxygen sensing-PLIM for metabolic mapping. *J Biophotonics* 9: 800–811

Kikuta J, Wada Y, Kowada T, Wang ZE, Sun-Wada G-H, Nishiyama I, Mizukami S, Maiya N, Yasuda H, Kumanogoh A *et al* (2013) Dynamic visualization of RANKL and Th17-mediated osteoclast function. *J Clin Invest* 123: 866–873

Kim K, Kim JH, Lee J, Jin HM, Kook H, Kim KK, Lee SY, Kim N (2007) MafB negatively regulates RANKL-mediated osteoclast differentiation. *Blood* 109: 3253–3259

Krab K, Kempe H, Wikstrom M (2011) Explaining the enigmatic K(M) for oxygen in cytochrome c oxidase: a kinetic model. *Biochim Biophys Acta* 1807: 348–358

Langmead B, Salzberg SL (2012) Fast gapped-read alignment with Bowtie 2. *Nat Methods* 9: 357–359

Laukka T, Mariani CJ, Ihantola T, Cao JZ, Hokkanen J, Kaelin Jr WG, Godley LA, Koivunen P (2016) Fumarate and succinate regulate expression of hypoxia-inducible genes via TET enzymes. *J Biol Chem* 291: 4256–4265

Lee WC, Guntur AR, Long F, Rosen CJ (2017) Energy metabolism of the osteoblast: implications for osteoporosis. *Endocr Rev* 38: 255–266

Lienhard M, Grimm C, Morkel M, Herwig R, Chavez L (2014) MEDIPS: genome-wide differential coverage analysis of sequencing data derived from DNA enrichment experiments. *Bioinformatics* 30: 284–286

Lorenzo J, Horowitz M, Choi Y (2008) Osteoimmunology: interactions of the bone and immune system. *Endocr Rev* 29: 403–440

Maeda K, Kobayashi Y, Udagawa N, Uehara S, Ishihara A, Mizoguchi T, Kikuchi Y, Takada I, Kato S, Kani S *et al* (2012) Wnt5a-Ror2 signaling between osteoblast-lineage cells and osteoclast precursors enhances osteoclastogenesis. *Nat Med* 18: 405–412

Majmundar AJ, Wong WJ, Simon MC (2010) Hypoxia-inducible factors and the response to hypoxic stress. *Mol Cell* 40: 294–309

Maxwell PH, Wiesener MS, Chang GW, Clifford SC, Vaux EC, Cockman ME, Wykoff CC, Pugh CW, Maher ER, Ratcliffe PJ (1999) The tumour suppressor protein VHL targets hypoxia-inducible factors for oxygen-dependent proteolysis. *Nature* 399: 271–275

Miyauchi Y, Ninomiya K, Miyamoto H, Sakamoto A, Iwasaki R, Hoshi H, Miyamoto K, Hao W, Yoshida S, Morioka H *et al* (2010) The Blimp1-Bcl6 axis is critical to regulate osteoclast differentiation and bone homeostasis. *J Exp Med* 207: 751–762

Mizukami K, Katano A, Shiozaki S, Yoshihara T, Goda N, Tobita S (2020) *In vivo* O2 imaging in hepatic tissues by phosphorescence lifetime imaging microscopy using Ir(III) complexes as intracellular probes. *Sci Rep* 10: 21053

Morimoto A, Kikuta J, Nishikawa K, Sudo T, Uenaka M, Furuya M, Hasegawa T, Hashimoto K, Tsukazaki H, Seno S *et al* (2021) SLPI is a critical mediator that controls PTH-induced bone formation. *Nat Commun* 12: 2136

Morita S, Kojima T, Kitamura T (2000) Plat-E: an efficient and stable system for transient packaging of retroviruses. *Gene Ther* 7: 1063–1066

Murata K, Fang C, Terao C, Giannopoulou EG, Lee YJ, Lee MJ, Mun SH, Bae S, Qiao Y, Yuan R *et al* (2017) Hypoxia-sensitive COMMD1 integrates signaling and cellular metabolism in human macrophages and suppresses osteoclastogenesis. *Immunity* 47: 66–79

Nakano M, Imamura H, Nagai T, Noji H (2011) Ca(2)(+) regulation of mitochondrial ATP synthesis visualized at the single cell level. *ACS Chem Biol* 6: 709–715

Nishikawa K, Nakashima T, Hayashi M, Fukunaga T, Kato S, Kodama T, Takahashi S, Calame K, Takayanagi H (2010) Blimp1-mediated repression of negative regulators is required for osteoclast differentiation. *Proc Natl Acad Sci USA* 107: 3117–3122

Nishikawa K, Iwamoto Y, Ishii M (2013) Development of an *in vitro* culture method for stepwise differentiation of mouse embryonic stem cells and induced pluripotent stem cells into mature osteoclasts. *J Bone Miner Metab* 32: 331–336

Nishikawa K, Iwamoto Y, Kobayashi Y, Katsuoka F, Kawaguchi S, Tsujita T, Nakamura T, Kato S, Yamamoto M, Takayanagi H *et al* (2015) DNA methyltransferase 3a regulates osteoclast differentiation by coupling to an S-adenosylmethionine-producing metabolic pathway. *Nat Med* 21: 281–287

Nishikawa K, Ishii M (2021) Novel method for gain-of-function analyses in primary osteoclasts using a non-viral gene delivery system. *J Bone Miner Metab* 39: 353–359

Ohh M, Park CW, Ivan M, Hoffman MA, Kim TY, Huang LE, Pavletich N, Chau V, Kaelin WG (2000) Ubiquitination of hypoxia-inducible factor requires direct binding to the beta-domain of the von Hippel-Lindau protein. *Nat Cell Biol* 2: 423–427

Okuno D, Sugiura Y, Sakamoto N, Tagod MSO, Iwasaki M, Noda S, Tamura A, Senju H, Umeyama Y, Yamaguchi H *et al* (2020) Comparison of a novel bisphosphonate prodrug and zoledronic acid in the induction of cytotoxicity in human Vgamma2Vdelta2 T cells. *Front Immunol* 11: 1405

Palazon A, Goldrath AW, Nizet V, Johnson RS (2014) HIF transcription factors, inflammation, and immunity. *Immunity* 41: 518–528

Ramasamy SK, Kusumbe AP, Wang L, Adams RH (2014) Endothelial Notch activity promotes angiogenesis and osteogenesis in bone. *Nature* 507: 376–380

Regan JN, Lim J, Shi Y, Joeng KS, Arbeit JM, Shohet RV, Long F (2014) Up-regulation of glycolytic metabolism is required for HIF1alpha-driven bone formation. *Proc Natl Acad Sci USA* 111: 8673–8678

Robinson MD, McCarthy DJ, Smyth GK (2010) edgeR: a Bioconductor package for differential expression analysis of digital gene expression data. *Bioinformatics* 26: 139–140

Roussakis E, Li Z, Nichols AJ, Evans CL (2015) Oxygen-sensing methods in biomedicine from the macroscale to the microscale. *Angew Chem Int Ed Engl* 54: 8340–8362

Rumsey WL, Vanderkooi JM, Wilson DF (1988) Imaging of phosphorescence: a novel method for measuring oxygen distribution in perfused tissue. *Science* 241: 1649–1651

Ryan HE, Lo J, Johnson RS (1998) HIF-1 alpha is required for solid tumor formation and embryonic vascularization. *EMBO J* 17: 3005–3015

Ryan HE, Poloni M, McNulty W, Elson D, Gassmann M, Arbeit JM, Johnson RS (2000) Hypoxia-inducible factor-1alpha is a positive factor in solid tumor growth. *Cancer Res* 60: 4010–4015

Sakaguchi Y, Nishikawa K, Seno S, Matsuda H, Takayanagi H, Ishii M (2018) Roles of enhancer RNAs in RANKL-induced osteoclast differentiation identified by genome-wide cap-analysis of gene expression using CRISPR/Cas9. *Sci Rep* 8: 7504

Semba H, Takeda N, Isagawa T, Sugiura Y, Honda K, Wake M, Miyazawa H, Yamaguchi Y, Miura M, Jenkins DM *et al* (2016) HIF-1alpha-PDK1 axis-induced active glycolysis plays an essential role in macrophage migratory capacity. *Nat Commun* 7: 11635

Semenza GL (2002) HIF-1 and tumor progression: pathophysiology and therapeutics. *Trends Mol Med* 8: S62–67

Solaini G, Baracca A, Lenaz G, Sgarbi G (2010) Hypoxia and mitochondrial oxidative metabolism. *Biochim Biophys Acta* 1797: 1171–1177

Spencer JA, Ferraro F, Roussakis E, Klein A, Wu J, Runnels JM, Zaher W, Mortensen LJ, Alt C, Turcotte R *et al* (2014) Direct measurement of local oxygen concentration in the bone marrow of live animals. *Nature* 508: 269–273

Sun-Wada GH, Tabata H, Kawamura N, Aoyama M, Wada Y (2009) Direct recruitment of H+-ATPase from lysosomes for phagosomal acidification. *J Cell Sci* 122: 2504–2513

Suzuki T, Uruno A, Yumoto A, Taguchi K, Suzuki M, Harada N, Ryoke R, Naganuma E, Osanai N, Goto A *et al* (2020) Nrf2 contributes to the weight gain of mice during space travel. *Commun Biol* 3: 496

Takayanagi H (2007) Osteoimmunology: shared mechanisms and crosstalk between the immune and bone systems. *Nat Rev Immunol* 7: 292–304

Tanaka S, Ise W, Inoue T, Ito A, Ono C, Shima Y, Sakakibara S, Nakayama M, Fujii K, Miura I *et al* (2020) Tet2 and Tet3 in B cells are required to repress CD86 and prevent autoimmunity. *Nat Immunol* 21: 950–961

Teitelbaum SL, Ross FP (2003) Genetic regulation of osteoclast development and function. *Nat Rev Genet* 4: 638–649

Thienpont B, Steinbacher J, Zhao H, D'Anna F, Kuchnio A, Ploumakis A, Ghesquiere B, Van Dyck L, Boeckx B, Schoonjans L *et al* (2016) Tumour hypoxia causes DNA hypermethylation by reducing TET activity. *Nature* 537: 63–68

Tsagaratou A, Rao A (2013) TET proteins and 5-methylcytosine oxidation in the immune system. *Cold Spring Harb Symp Quant Biol* 78: 1–10

Vanderkooi JM, Maniara G, Green TJ, Wilson DF (1987) An optical method for measurement of dioxygen concentration based upon quenching of phosphorescence. *J Biol Chem* 262: 5476–5482

Varia MA, Calkins-Adams DP, Rinker LH, Kennedy AS, Novotny DB, Fowler Jr WC, Raleigh JA (1998) Pimonidazole: a novel hypoxia marker for complementary study of tumor hypoxia and cell proliferation in cervical carcinoma. *Gynecol Oncol* 71: 270–277

Wang GL, Jiang BH, Rue EA, Semenza GL (1995) Hypoxia-inducible factor 1 is a basic-helix-loop-helix-PAS heterodimer regulated by cellular O2 tension. *Proc Natl Acad Sci USA* 92: 5510–5514

Wang GL, Semenza GL (1993) General involvement of hypoxia-inducible factor 1 in transcriptional response to hypoxia. *Proc Natl Acad Sci USA* 90: 4304–4308

Wang Y, Wan C, Deng L, Liu X, Cao X, Gilbert SR, Bouxsein ML, Faugere MC, Guldberg RE, Gerstenfeld LC *et al* (2007) The hypoxia-inducible factor alpha pathway couples angiogenesis to osteogenesis during skeletal development. *J Clin Invest* 117: 1616–1626

Wilson JW, Shakir D, Batie M, Frost M, Rocha S (2020) Oxygen-sensing mechanisms in cells. *FEBS J* 287: 3888–3906

Xie H, Cui Z, Wang L, Xia Z, Hu Y, Xian L, Li C, Xie L, Crane J, Wan M *et al* (2014) PDGF-BB secreted by preosteoclasts induces angiogenesis during coupling with osteogenesis. *Nat Med* 20: 1270–1278

Yamamoto M, Kim M, Imai H, Itakura Y, Ohtsuki G (2019) Microglia-triggered plasticity of intrinsic excitability modulates psychomotor behaviors in acute cerebellar inflammation. *Cell Rep* 28: 2923–2938

Yamazaki S, Souma T, Hirano I, Pan X, Minegishi N, Suzuki N, Yamamoto M (2013) A mouse model of adult-onset anaemia due to erythropoietin deficiency. *Nat Commun* 4: 1950

Yona S, Kim KW, Wolf Y, Mildner A, Varol D, Breker M, Strauss-Ayali D, Viukov S, Guilliams M, Misharin A *et al* (2013) Fate mapping reveals origins and dynamics of monocytes and tissue macrophages under homeostasis. *Immunity* 38: 79–91

Yoshihara T, Hosaka M, Terata M, Ichikawa K, Murayama S, Tanaka A, Mori M, Itabashi H, Takeuchi T, Tobita S (2015) Intracellular and *in vivo* oxygen sensing using phosphorescent Ir(III) complexes with a modified acetylacetonato ligand. *Anal Chem* 87: 2710–2717

Zaidi M (2007) Skeletal remodeling in health and disease. *Nat Med* 13: 791–801